이학석사 학위논문

Spatial Variation and Frequency Dependence of Lg Wave Attenuation with Site Response Correction Along the CCSE Array in Central California, US

미국 캘리포니아 지역의 CCSE 관측망에서의

Lg파 감쇠현상의 공간적 변화 및

부지 응답 보정, 그리고 주파수 의존성

2021년 2월

서울대학교 대학원

지구환경과학부

윤 지 나

Spatial Variation and Frequency Dependence of Lg Wave Attenuation with Site Response Correction Along the CCSE Array in Central California, US

지도 교수 김 영 희

이 논문을 이학석사 학위논문으로 제출함
2020년 12월

서울대학교 대학원
지구환경과학부
윤 지 나

윤지나의 이학석사 학위논문을 인준함
2021년 1월

위 원 장 _____ 이 준 기 _____ (인)

부위원장 _____ 김 영 희 _____ (인)

위 원 _____ 강 태 섭 _____ (인)

Abstract

We estimate lateral variation of the *Lg Q* at four center frequencies, 0.75 Hz, 1 Hz, 2 Hz and 2.75 Hz, based on the two-station method (TSM) along a great circle profile (A–A') passing the Central California Seismic Experiment (CCSE) array. Relative site responses at each station are also obtained using the reverse two-station method.

Positive site responses are obtained from 34 stations out of total 46 stations examined, and their responses are mostly correlated with geological features (i.e. sedimentary rocks) along the profile. Surficial lithology is likely to have a significant impact on the site response, rather than the thickness of sediments. The site responses also exhibit strong negative correlation to the V_{S30} data.

We then correct the *Lg Q* estimates for the site responses. The correction is effective in eliminating surficial properties, resulting in a shift of the peak locations, being more remarkable at lower frequencies (0.75 Hz and 1 Hz) than at higher frequencies (2 Hz and 2.75 Hz). With the site-response-corrected Q values, a power-law frequency dependence of $\boldsymbol{Q(f) = (81 \pm 8)f^{(0.62 \pm 0.11)}}$ is obtained, reflecting the active tectonic setting and the presence of fluids in the region. We also compared the corrected *Lg Q* variation with several geologic properties. The effect of sediments becomes trivial after the correction, particularly at lower frequencies. Comparison to the V_S and Moho temperature showed that each frequency is capable of imaging distinct depth range.

Finally, we compare the result to that of the Sacramento Valley. An analogous behavior at the sedimentary basin is obtained at both regions. However, the

conflicting result in Sierra Nevada emphasizes a necessity of further investigation in

the region with denser seismic networks.

Contents

List of Figures

List of Tables

Chapter 1

Introduction

Lg wave is well known as the most prominent phase in high frequency seismograms that traveled through a continental path. The *Lg* is often modeled either as a sum of higher mode surface waves (Oliver and Ewing, 1954; Knopoff et al., 1973) or as a superposition of critically reflected *S*-waves (Bouchon, 1982). The *Lg* is fully developed at regional distances (200 – 1500 km), and is hard to distinguish from the *Sg* phase at local distances ($\leq$ 200 km) (Kennett, 1983; Xie and Mitchell, 1990b) or even becomes incoherent at teleseismic distances (Gallegos et al., 2017). Typically, the *Lg* phase propagates with group velocities ranging from 3.0 to 3.6 km/s in western US (Xie and Mitchell, 1990b; Phillips and Stead, 2008; Gallegos et al., 2017).

Kennett (1986) reported that the *Lg* wave dissipates significantly into other phases such an *Sn* as the crust gets thinner and concluded that the *Lg* wave can only

propagate on the continental path. This restriction in pathway makes it powerful for imaging continental structures since there is little chance of oceanic contamination. In the virtue of its uniqueness, the *Lg* is utilized in diverse field of seismic investigations such as magnitude measurement (m_b (*Lg*); Nuttli, 1973; Zhao et al., 2008) or discrimination between natural earthquakes and manmade explosions at regional distances (Blandford, 1981). Mapping crustal heterogeneities with *Lg* wave attenuation has also been one of the major applications and performed by a number of studies in various regions such as continental US, China, and Australia (Hasegawa, 1985; Xie and Mitchell, 1990a, b; Xie et al., 2004; Noriega et al., 2015; He et al., 2017; Wei et al., 2017).

The quality factor Q is an index which measures the efficiency of wave propagation and inversely proportional to the attenuation coefficient. *Lg* is very useful for Q studies, because it can easily be identified even for a small-magnitude event owing to its large amplitude, and is almost always present in the seismogram of continental path. Thus, the data has been used for constraining crustal properties in tectonically active region. *Lg* Q is often more sensitive than the seismic velocity (Nuttli, 1973), and at 1 Hz (i.e., *Lg* Q_0), it is well known to have a strong correlation with tectonic activities, being large at tectonically stable areas such as cratons and small at tectonically active areas. Particularly, Q_0 value is highly sensitive to the variation of temperature and presence of fluid. Such observed properties make *Lg* Q more useful when studying regional variation of the crustal structure and provide key constraints on material properties and structure.

Among several methods that are available for estimating the *Lg* attenuation, two-station method (TSM), initially suggested by Tsai and Aki (1969), is widely used since it can suppress site and source effect by using a ratio from a two-station pair

(Xie et al., 2004 – Tibet; Noriega et al., 2015 – Iberian Peninsula; He et al., 2017 – eastern Mongolia; Wei et al., 2017 – Australia; Gallegos et al., 2017 – western US). Reverse two-station method (RTSM) exploits two events simultaneously recorded at two stations, eliminates site terms nearly completely, which results in better accuracy than the TSM. Ford et al. (2008) compared five methods of estimating $Lg\ Q$ and reported relatively low dependence on parameter selection for both TSM and RTSM. They asserted that the TSM is sensitive to the selection of frequency band while RTSM is nearly undisturbed by parameter selection. However, the strict geometry requirement of RTSM greatly reduces the quantity of available dataset. Therefore, we adopt the TSM for the investigation of $Lg\ Q$ and use RTSM only for the estimation of relative site responses.

There are several previous studies on $Lg\ Q$ structure for western US conducted with various methods to investigate its complex geology (Table 1). Singh and Herrmann (1983) and Baqer and Mitchell (1998) estimated Lg coda Q for the entire US, using a scattering model and stacked spectral ratio method, respectively. Both studies reported low Q value of 140–200 and 250–300 for western US. Benz et al. (1997) estimated the frequency dependence of $Lg\ Q$ for several sub-regions in continental US by inverting the Lg wave amplitude into source terms, site terms and $Lg\ Q$ through singular value decomposition for every octave between 0.5 and 7.0 Hz. For southern-central California, $Q(f) = (187 \pm 7)f^{(0.55\pm0.03)}$ is obtained between 1.0 and 7.0 Hz. More recently, Erickson et al. (2004) determined the frequency dependence of $Lg\ Q$ for the continental US centering at 0.75, 1.0, 3.0, 6.0 and 12.0 Hz. They inverted the Lg wave amplitude data with singular value decomposition and yielded the frequency dependent Lg attenuation being $Q(f) = (105 \pm 26)f^{(0.67\pm0.16)}$ and $Q(f) = (152 \pm 37)f^{(0.68\pm0.12)}$ for northern and

southern California, respectively. Phillips and Stead (2008) provided a high-resolution 2-D map of 1-Hz Lg attenuation for western US with Q values within the range of 100–300 in Central California. They reported association of high Q with stable cratons or intrusive igneous batholiths (e.g., Colorado and Columbia Plateaus, Sierra Nevada) and low Q with tectonically active regions (e.g., coastal California, Yellowstone). Mitchell et al. (2015) obtained a continent-wide Lg coda Q tomography map at 1 Hz and its frequency dependence using the stacked spectral ratio method. Q_0 values were predominantly low along the western coast (200–350) and gradually increased toward east, being the highest at the Canadian Shield. Gallegos et al. (2017) estimated $Lg\ Q$ and relative site responses in western US using the TSM and RTSM, respectively, at four different frequencies (0.5, 1, 2 and 3 Hz). The results show similar Q variations with that of Phillips and Stead (2008) at 1 Hz, with frequency dependence of $Q(f) = 97f^{0.25}$ and $Q(f) = 99f^{0.44}$ for southern and northern California, respectively. Although they provided a map of relative site responses, they did not interpret the westernmost part of the US due to the low resolution. Yassminh et al. (2019) adopted the RTSM to obtain site responses at central-eastern US, using the Lg wave. They reported a strong correlation of the site responses to the basins and sediments, the topography of the region and the surface shear-wave velocity (i.e., V_{S30}). However, large-scale studies focusing on contiguous US or entire western US frequently lack the resolution at westernmost end of US since the region falls within the edge of inversion grids. For this reason, there is only scarce or no detailed study on the region despite its complex crustal characteristics.

In this study, we investigate lateral variation and frequency dependence in crustal $Lg\ Q$ along a great circle profile in westernmost part of the US, using the dense seismic array data acquired from Central California Seismic Experiment

(CCSE). To take full advantage of the dense linear array, we focus on one-dimensional lateral variation of *Lg Q* beneath the array with the highest resolution using the TSM and RTSM rather than two-dimensional tomography approach. Investigation of the lateral *Lg Q* variations along the array is invaluable in that it crosses several geologically important features such as a major plate-boundary fault (i.e., the San Andreas Fault), thick sedimentary basin (i.e., the Central Valley) and massive mountain ranges (i.e., Sierra Nevada). Moreover, basements beneath the CCSE array also vary from metasedimentary Franciscan Complex (Bennington et al., 2008) to igneous Sierra Nevada batholith (Godfrey and Klemperer, 1998). Along with the *Q* structure, we obtain relative site responses at each station to consider the effect of site amplification, and use the estimates to correct the *Lg Q* structure. Through the study, we aim to provide deeper insight into the nature of *Lg Q* attenuation with the known geologic features and also in the considered frequency range.

Table 1. *Q* values reported from previous studies for western US.

Reference	$Q(f)$ for western US	Seismic Phase	Frequency Range (Hz)	Study Area
Singh & Herrmann (1983)	140–200	*Lg* Coda	0.5–3.5	Entire US
Benz et al. (1997)	$(187\pm7)f^{(0.55\pm0.03)}$ [*]	*Lg*	1.0–7.0	Continental US
Baqer & Mitchell (1998)	250–300	*Lg* Coda	1.0	Continental US
Erickson et al. (2004)	$(152\pm37)f^{(0.72\pm0.16)}$ [*] $(105\pm26)f^{(0.62\pm0.16)}$ [**]	*Lg*	0.75, 1.5, 3.0, 6.0, 12.0	Continental US
Phillips & Stead (2008)	80–200	*Lg*	1.0	Western US
Mitchell et al. (2015)	200–350	*Lg*	1.0	Entire US
Gallegos et al. (2017)	$97f^{0.25}$ [*] $99f^{0.44}$ [**]	*Lg*	0.5, 1.0, 2.0, 3.0	Western US

[*] Estimated for southern California
[**] Estimated for northern California

Chapter 2

Geological Setting

The CCSE array extends from the Pacific coast to the Sierra Nevada foothills in east-west direction, crossing several geologically unique features: the creeping section of the San Andreas Fault (SAF) and 100-km wide Central Valley forearc basin (CV; Fig. 1). The SAF is a vast, right-lateral strike slip fault system traversing the western coast of the US. Although direct causal relationship between the SAF and the $Lg\ Q$ has not been established yet, the SAF can affect the value since it can be a channel for fluid migration. Moreover, several geophysical evidences such as a sharp contrast of P-wave velocity structure (Eberhart-Phillips and Michael, 1993) illustrate that the fault zone can act as a boundary of two distinct basements. The CV is a massive forearc basin, which is formed during the Mesozoic subduction of the Pacific Plate underneath the North American Plate. The basin is mainly filled with Quaternary alluvium and marine sediments (Jennings et al., 1977), most of which is

unconsolidated or loosely consolidated (Poland and Evenson, 1966; Farrar and Bertoldi, 1988). Generally, unconsolidated sedimentary layers are known to cause strong attenuation of the *Lg* wave, which leads to low *Lg Q* values (Mitchell and Hwang, 1987; Zhao et al., 2010; Hong et al., 2010; Wei et al., 2017; Zhao and Mousavi, 2018).

The deeper lithology beneath the CCSE array changes abruptly, transitioning from harder Salinian blocks into softer metasedimentary Franciscan complex (Page, 1981). The Salinian block is an aggregate of Cenozoic granitic and metamorphic rocks, which has been transported northwestward by the right-lateral movement of SAF. The block exhibits high resistivity (Unsworth and Bedrosian, 2004; Becken et al., 2008), high seismic velocity (Eberhart-Phillips and Michael, 1993; Zhang and Thurber, 2005), and high Q_P and Q_S values (Bennington et al., 2008; Eberhart-Phillips, 2016). The Franciscan complex is an accretionary wedge that is formed during the Mesozoic subduction. The effect of the Franciscan complex to the attenuation remains unclear: Bennington et al. (2008) speculated that the high Q values imaged by the body-wave attenuation tomography might be the result of the closure of cracks in the rocks of the complex, whereas Eberhart-Phillips (2016) reported moderately low Q value for the Franciscan complex from the *P*- and *S*-wave attenuation models.

Farther toward inland, a 10–12 km thick Great Valley Ophiolite (GVO) underlies the CV which is a mafic oceanic crust that has been obducted onto the continental crust during Jurassic Nevadan orogeny (Godfrey et al., 1997; Godfrey and Klemperer, 1998). The GVO is known to exhibit high Q imaged by body-wave attenuation tomography (Eberhart-Phillips et al., 2014; Eberhart-Phillips, 2016). At the easternmost part of our study region, there lies an old and stiff Sierran Basement,

which is mainly consisted of Mesozoic granitic rocks (Godfrey and Klemperer, 1998). High Q values are reported for the Sierren Basement from both body wave (Eberhart-Phillips et al., 2016) and Lg wave (Phillips and Stead, 2008; Gallegos et al., 2017) analyses.

In addition to complex crustal lithology, an eccentric seismic feature beneath the Central Valley is detected as high-velocity anomaly at upper mantle depth (>40 km), called the Isabella anomaly. Two main hypotheses are put forward as its tectonic origin: one asserts that the anomaly is a remnant fossil slab fragment (Pikser et al., 2012; Wang et al., 2013; Jiang et al., 2018) and the other claims that it is a foundered lithosphere that was detached from the Sierran Basement (Zandt et al., 2004; Boyd et al., 2004). However, its origin is not yet clarified. Considering that the Isabella anomaly can affect the composition of the lowermost crust and its origin can be highly relevant with local crustal evolution, we fully take the anomaly into account when interpreting the $Lg\ Q$ variation along the CCSE array.

Figure 1. Simplified geologic map of Central California (Jennings et al., 1977). Location of the CCSE array (black boxes) and the great circle profiles (A–A' and B–B') are marked on the map. Grey lines indicate faults (USGS). Rock type and associated color legends are shown below the figure. (SAF: San Andreas Fault zone)
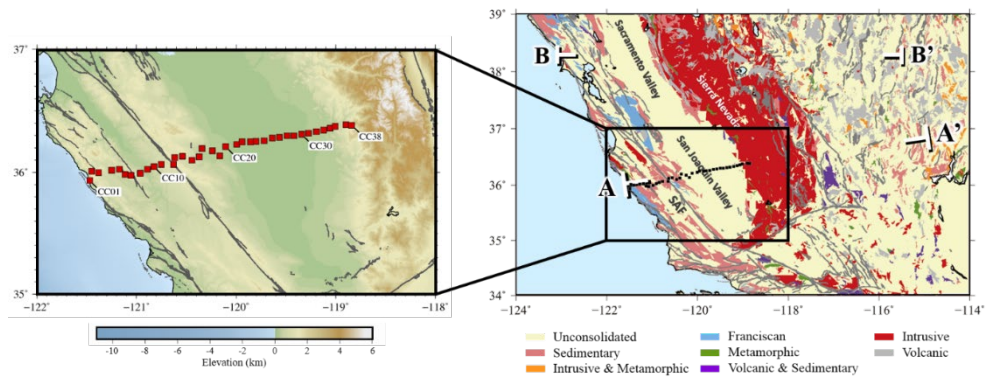
Chapter 3

Data Processing

We used 637 crustal earthquakes that occurred during Jan. 2013 – Dec. 2016 recorded by the CCSE array and Global Seismic Network (GSN) stations (Fig. 2). We selected 10 GSN stations that are located farther east to the CCSE array (Fig. 2). Data from the GSN stations greatly improved the spatial coverage. However, low station density of the GSN stations led to relatively lower resolution results compared to those obtained from the CCSE. The resolution problem is discussed in detail in the section 5.1. Among the CCSE stations, station CC36 showed anomalously low amplitudes with its peak amplitude lower by a factor of 20, compared to the nearby stations (i.e., CC35 and CC37) that are located only 4 – 5 km apart from the CC36. Thus we consider the station to have a gain problem and exclude its data for further investigation. Events are filtered primarily according to their location, and we only keep those events that have little or no chance of passing

oceanic paths. Also, events recorded for less than three stations are not used. After the screening, the number of events reduced down to 531. In order to ensure the generation of *Lg* wave, we only retained seismic records with epicentral distance larger than 250 km with maximum distance being 1,946 km. The magnitude of the events ranges from 3.5 to 6.1. We band-pass filtered seismograms with bandwidths of 0.375 – 1.125 Hz, 0.5 – 1.5 Hz, 1.0 – 3.0 Hz, and 1.375 – 4.125 Hz centering at 0.75 Hz, 1 Hz, 2 Hz, and 2.75 Hz, respectively. Then the mean, trend and instrumental responses are removed. Fig. 3 shows a record section of one earthquake that shows clear development of the *Lg* phase. The stations are either broadband or high broadband, and only vertical component is used. Only those stations that recorded more than three events are left, which resulted in total 37 CCSE array stations (CC01 – CC38; except CC36) and 9 GSN stations (Table 2).

To control the quality of the data, each seismogram is separated into two windows: *Lg* window and noise window. The window for *Lg* wave is automatically determined to have a length of 0.6 km s^{-1}, beginning from group velocity of 3.6 km s^{-1} and terminating at the point where group velocity becomes 3.0 km s^{-1}. Group velocity values for the starting and ending points are chosen based on previously reported values (i.e., Phillips and Stead, 2008; Zhao et al., 2013b; Gallegos et al., 2017). The noise refers to pre-*P* noise, whose window is defined to have the same length with the *Lg* window and terminates at the first *P*-wave arrival (Fig. 4). We add 10% buffer to either side of both windows to complement minor fluctuation in actual wave arrival.

For strict control on the quality of data, we apply two methods based on signal-to-noise ratio (SNR): one using root mean square (RMS) amplitude in time domain and the other using Fourier transformed spectra in frequency domain. First,

12

we excluded events if the ratio of RMS amplitude of *Lg* window to the RMS amplitude of noise window is lower than 2 (Fig. 4). For those events that passed RMS SNR criteria, both *Lg* and noise windows are transformed into frequency domain via Fast Fourier Transformation (FFT) with 20% cosine taper window (Fig. 5b). Frequency content resulting from the FFT is denser at higher frequencies and sparser at lower frequencies. Therefore, we define the reference frequencies to have a length of 58 and log-evenly distributed from 0.05 Hz to 10.0 Hz and used spectral values on these frequencies for the SNR analysis following the approach taken by Zhao et al. (2010). Power spectral amplitudes are then estimated by either Lagrangian interpolation after 3-point running average smoothing for lower frequencies ($\leq$0.5 Hz) (Xie and Mitchell, 1990b), and the same method as that describe in section 3.1. of Zhao et al. (2010) for higher frequencies ($\geq$0.5 Hz). Assuming 1) the raw *Lg* spectra contain both pure *Lg* and noise component and 2) the two are independent from each other, spectral amplitude of pure *Lg* wave can be estimated using the relationship: $A_{pure}^2(f) = A_{raw}^2(f) - A_{noise}^2(f)$ where A denotes the amplitude in frequency domain. By taking the ratio of the spectral amplitudes of the pure *Lg* and noise, we calculate the SNR and data with SNR > 2 are used while others are excluded for further steps (Fig. 5c).

Figure 2. Location of earthquakes and stations used in this study. Squares and circles indicate seismic stations and earthquake epicenters, respectively. Red squares represent the CCSE array while white and green represent GSN stations. The event marked with the white arrow (event 150727_M4.4) and the station filled in green (HEL) are referred in the example shown in Fig. 7.
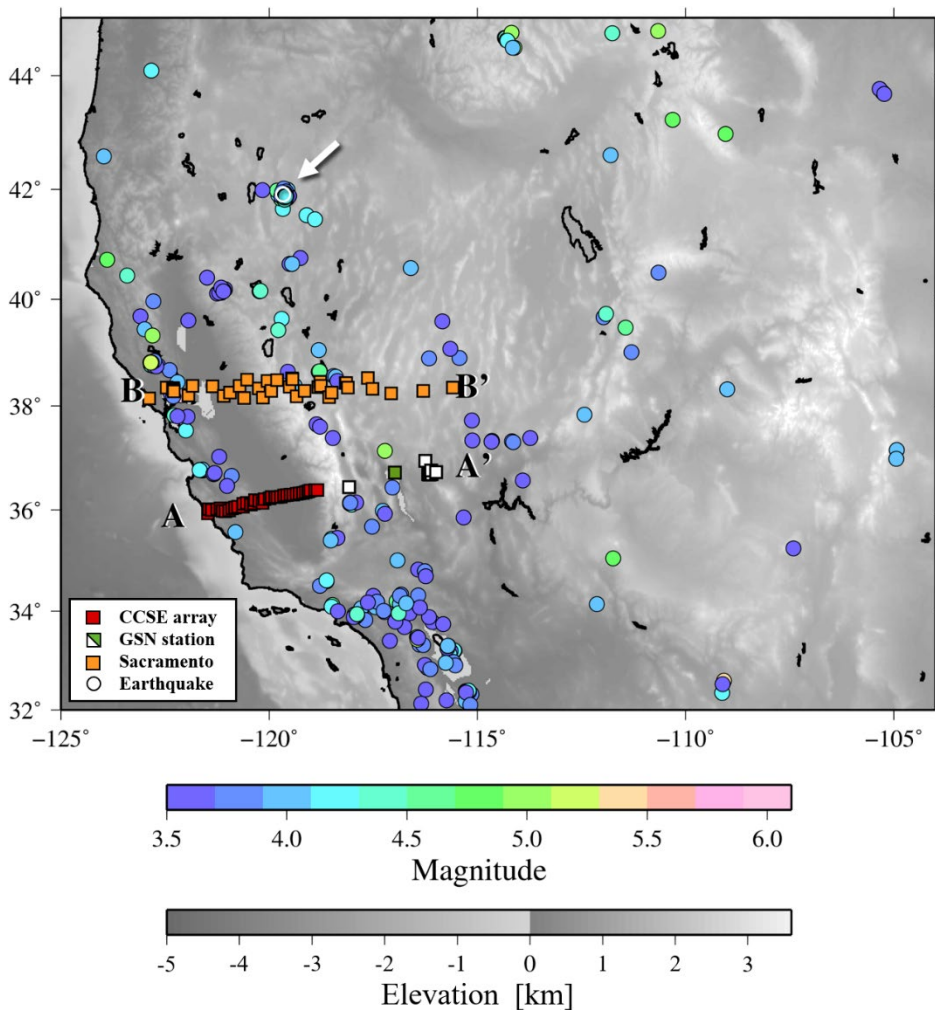
Figure 3. Record section showing vertical-component seismograms for an M5.0 event. Origin time and magnitude of this example earthquake are shown on the top. Seismograms are band-pass filtered with corner frequencies of 0.5 – 1.5 Hz, centering at 1 Hz. Light-blue solid lines across the record section represent apparent group velocity of 3.0 and 3.6 km/s, which will be used as a *Lg* window for later analysis. Pink shaded area indicates location of the San Andreas Fault.

2015-05-22T18.47.43.200 M5.0
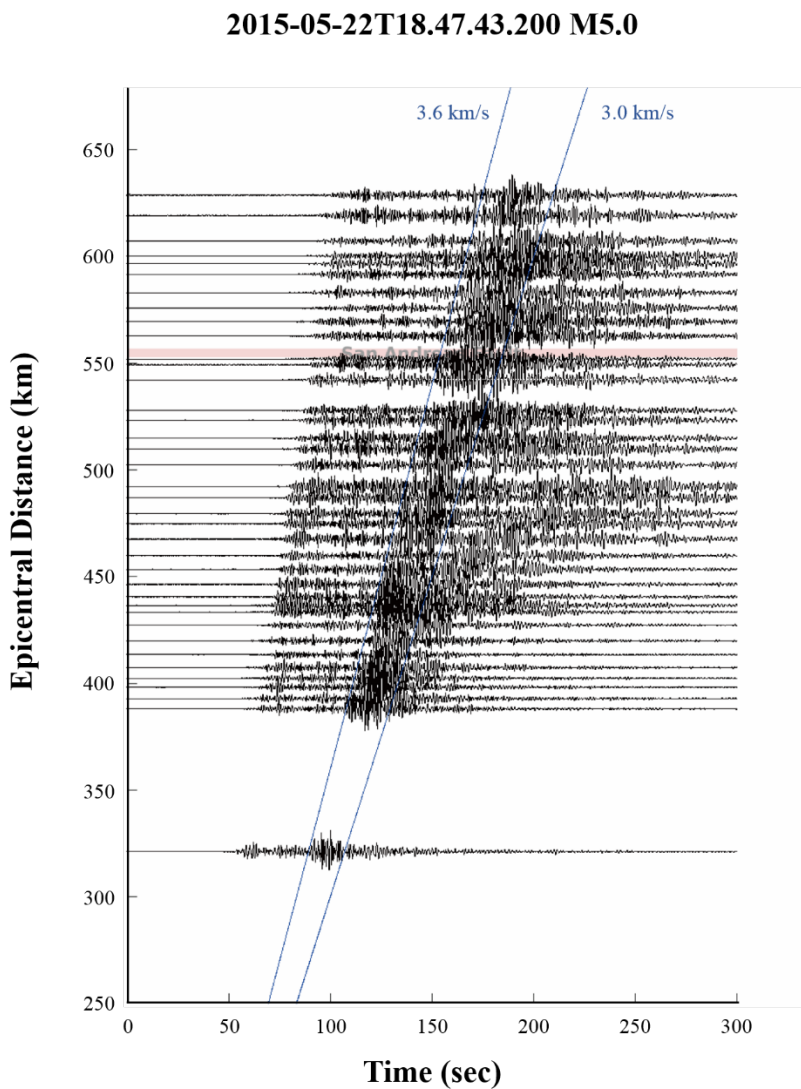
Figure 4. Process of SNR screening based on RMS amplitude (at 1 Hz). This figure shows two recordings which did (a) and did not (b) pass the RMS SNR criterion. Estimated RMS SNR value is 10.85 and 0.96 for (a) and (b), respectively. Pink shaded area indicates *Lg* window and green shaded area represents noise window in each case.
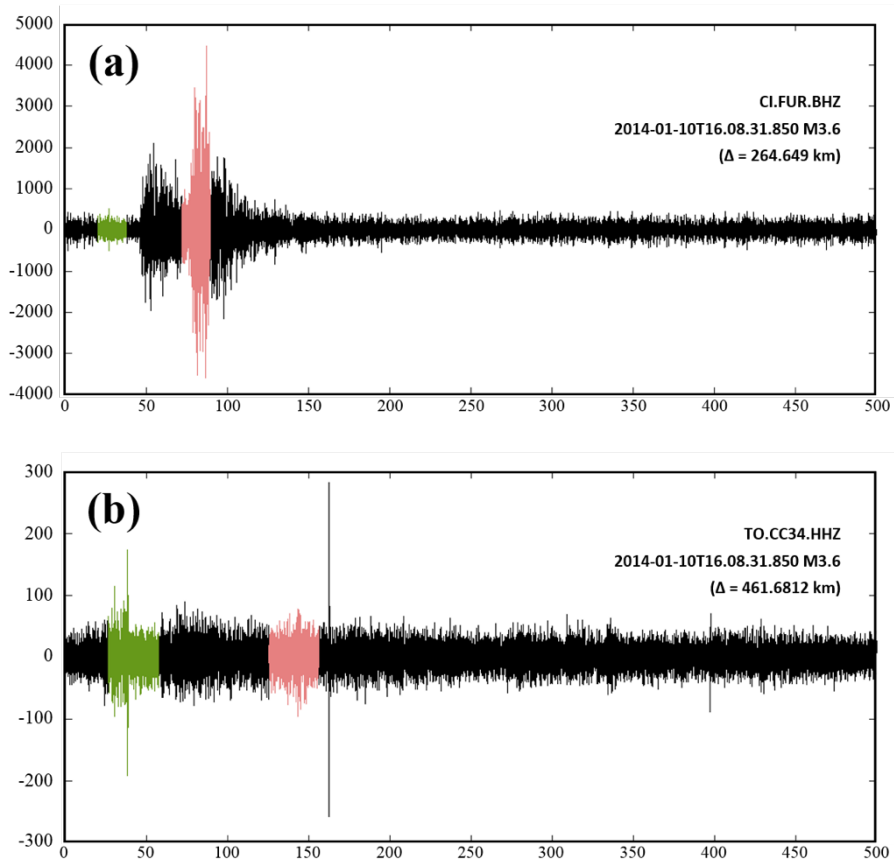
Figure 5. Process of the SNR screening in frequency domain (at 1 Hz). (a) An example of a seismogram recorded from station HEL (Fig. 2, green square) with both noise (blue) and *Lg* (pink) windows. (b) Fourier transformed spectra for both *Lg* and noise windows. Open circles and triangles denote log-evenly distributed reference points with spectral values for the two phases. (c) SNR values at reference frequencies. Pink shaded area represents signals with SNR of > 2, and we discard the data with SNR less than 2.
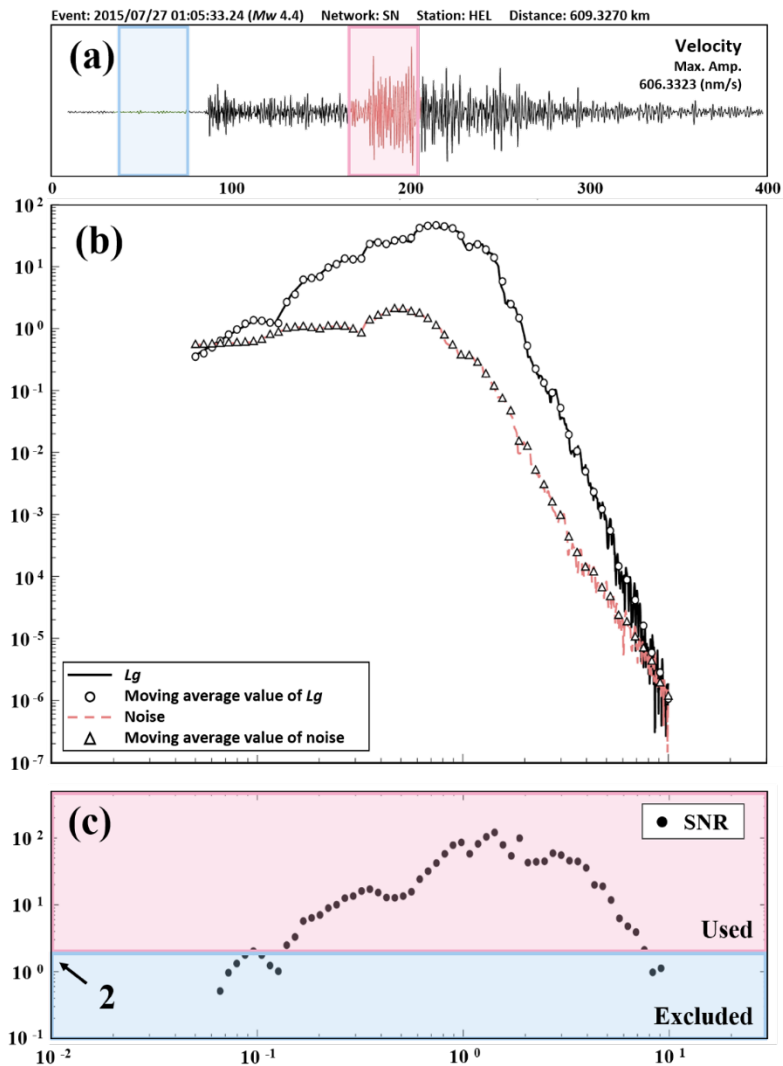
Table 2. GSN stations used in this study.

Network	Station	Longitude (deg.)	Latitude (deg.)
CI	CWC	-118.08	36.44
	VOG	-119.38	36.32
SN	HEL	-116.98	36.72
	JFR2	-116.15	36.69
	RVFF	-116.11	36.76
	RVNE	-116.10	36.70
	RVSE	-115.99	36.73
	SPRS	-116.18	36.69
	TPNV	-116.25	35.95

Chapter 4

Methods

To investigate lateral variations of *Lg Q* along a great circle profile (A–A') we first chose two-station pairs satisfying azimuthal and back-azimuthal difference criteria ($\delta\theta < 15°$). For all possible two-station pairs, interstation *Lg Q* values are measured using the two-station method (TSM). We then divided the profile into several cells, assuming that the *Q* value inside each cell is uniform. Finally, we inverted the interstation *Lg Q* values into the *Q* values in each cell, using the Levenberg-Marquardt method (Levenberg, 1944; Marquardt, 1963). In addition, relative site responses at each station are estimated by the reverse two-station method (RSTM). Details for each step are described in the subsequent sub-sections.

4.1. Two-Station Method (TSM)

In general, the spectral amplitude $A(f, \Delta)$ recorded on a station can be represented as below:

$$A(f, \Delta) = S(f)I(f)E(f)G(\Delta)exp\left(\frac{-\pi f \Delta}{v_{Lg}Q(f)}\right) \tag{1}$$

where f refers to the frequency, Δ refers to the epicentral distance, v_{Lg} refers to the Lg wave group velocity (3.5 km s^{-1}), S refers to the source spectrum, I refers to the instrumental response at the station, E refers to the site response, and Q refers to the frequency-dependent quality factor. The geometrical spreading $G(\Delta)$ can be expressed with a constant G_0 and geometrical spreading coefficient m as follows:

$$G(\Delta) = G_0 \Delta^{-m}. \tag{2}$$

Based on previous studies, it is valid to assume $m = 0.5$ provided that epicentral distance is large enough to produce the Lg wave (> 250 km) (Yang, 2002). Since we only use epicentral distances larger than 250 km, we adopt the value in our study. From equation (1) and (2), the ratio of spectral amplitudes from two stations (station 1 and 2) recording the same event (event a) can be expressed as:

$$\frac{A_{1a}}{A_{2a}} = \frac{S_a E_1 I_1 \Delta_{1a}^{-m}}{S_a E_2 I_2 \Delta_{2a}^{-m}} exp\left(\frac{-\pi f(\Delta_{1a} - \Delta_{2a})}{v_{Lg}Q(f)}\right). \tag{3}$$

In an ideal TSM geometry (Fig. 6a), an event and a two stations pair should lie strictly on a great circle profile. However, in reality, such ideal geometry can be hardly achieved and thus azimuthal difference from the two stations ($\delta\theta$) is often non-zero (Fig. 6b). Deviation from the perfect linear geometry gives rise to potential errors in Q estimates since non-isotropic source radiation can affect the result and

20

information outside the profile might also be included. However, Der et al. (1984) reported that such errors can be minimized when $\delta\theta$ is less than 15°. Along with the azimuthal difference criteria, Gallegos et al. (2017) applied stronger criteria regulating back-azimuthal difference to be also less than 15°. Hence, we constrained both the azimuthal and back-azimuthal deviation to be less than 15°. Instrumental response I is removed during the data processing stage. Since two stations are recording the same event and have nearly identical azimuths, source spectra S can also be eliminated. Then equation (3) can be simplified as:

$$\frac{v_{Lg}}{\pi\Delta_{12}}\ln\left[\frac{E_2 A_{1a}\Delta_{1a}^m}{E_1 A_{2a}\Delta_{2a}^m}\right] = \frac{f}{Q(f)} \tag{4}$$

where $\Delta_{12} = \Delta_2 - \Delta_1$. In conventional TSM, the two rays are assumed to travel through similar paths and thus the ratio of E_1 to E_2 is regarded as unity. However, we assess the validity of the assumption of uniform site responses since geologic properties along the great circle profile in our study region vary rapidly in a relatively short distance range. Therefore, we correct for the site response term by substituting E_1 and E_2 values with the estimates from the RTSM, and compare the result with that from the conventional TSM. For both cases, we estimate Q value at desired center frequency by fitting discrete left-hand side values of the equation (4) into a curve. Curve fitting is performed by the Levenberg-Marquardt method (Levenberg, 1944; Marquardt, 1963), which will be described in detail later in this section.

Relative error in estimating interstation Q value can be estimated by equation (5), as suggested by Xie et al. (2004):

$$\frac{\delta Q}{Q} = \frac{v_{Lg}}{f\pi}\left(\frac{Q}{\Delta_{12}}\right)\delta x \tag{5}$$

where δQ is the error in interstation Q measurement and δx is a small term expressing

the level of modeling error, assumed to have a value of 0.2 in this study. Since the interstation distance Δ_{12} is in the denominator, it is important to regulate minimum interstation distance to ensure low level of relative error. In this study, we discarded the pairs having interstation distance shorter than 30 km. Additionally, we kept Q estimates only when its value lies between the range of 10 – 2000 and the level of the relative error ($\delta Q/Q$) is less than 0.4. To screen out extreme Q values, we excluded the estimates if they were larger than 1.5 times the standard deviation.

After the interstation Q value is obtained for all possible two-station pairs, we segmented the great circle profile into several cells (A–A' in Fig. 7). Assuming that Q value is uniform within the cell, we can estimate the representative Q value for the mth cell ($m = 1, 2, \ldots , M$) as Q_m by following linear relationship:

$$\frac{\Delta_n}{Q_n} = \sum_{m=1}^{M} \frac{\Delta_{mn}}{Q_m} \tag{6}$$

where Δ_n is an interstation distance for the nth ray ($n = 1, 2, \ldots, N$), Q_n is the interstation Q value for the nth ray, and Δ_{mn} is the length of the nth ray passing through the mth cell. Equation (6) can then be represented by a linear system $\mathbf{d} = \mathbf{Gm}$, where $\mathbf{d}$ is a N-by-1 column vector consisting of the left-hand side of the equation (6), $\mathbf{G}$ is N-by-M matrix composed by Δ_{mn} values and $\mathbf{m}$ is a M-by-1 column vector having values of $1/Q_m$. The system can be solved iteratively using the least squares scheme based on the Levenberg-Marquardt method (Levenberg, 1944; Marquardt, 1963). We used a MATLAB code package designed and distributed by Gavin (2019). In order to prevent extreme values, we imposed a moderate smoothing step into the inversion process by the following equation:

$$\text{new}Q_m = \frac{1}{12}[Q_{m-1} + 10Q_m + Q_{m+1}]. \tag{7}$$

We found that the choice of an initial damping parameter λ and the associated factors for increasing/decreasing λ for every step can largely affect the inversion result. Among numerous trials, the damping factor used by Madsen et al. (2004) produced the most stable result. Let $\boldsymbol{A_0} = \boldsymbol{J^T J}$ with $\boldsymbol{J}$ being Jacobian matrix of the given system, then the initial value is related to the maximum diagonal component of $\boldsymbol{A_0}$ as followings:

$$\lambda_0 = \tau \cdot \max_i \left\{ a_{ii}^{(0)} \right\} \tag{8}$$

where τ is a constant chosen by user, typically suggested to have a value of 10^{-6} – 10^{-3}, or even 10^0 when initial guess is thought to be close to final result. We searched for the optimal value of τ by incrementally increasing the value from 10^{-6} to 10^0. The value that resulted in minimal residual with the input data is automatically chosen during the inversion process.

4.2. Revers Two-Station Method (RTSM)

Unlike the TSM, the RSTM utilizes a pair of two stations and two events aligning almost linearly (Fig. 6c). For two stations *1* and *2* that record two events *a* and *b*, the spectral amplitude ratio can be present in several forms:

$$\frac{A_{1a}A_{1b}}{A_{2a}A_{2b}}$$

$$= \left(\frac{E_1 I_1}{E_2 I_2}\right)^2 \left(\frac{\Delta_{1a}\Delta_{1b}}{\Delta_{2a}\Delta_{2b}}\right)^{-m} exp\left(\frac{\pi f(\Delta_{2a} - \Delta_{1a} + \Delta_{2b} - \Delta_{1b})}{v_{Lg}Q(f)}\right) \quad (8)$$

as presented by Chun et al. (1987) and Gallegos et al. (2017), or in the form of:

$$\frac{A_{1a}A_{2b}}{A_{2a}A_{1b}}$$

$$= \left(\frac{E_1 E_2}{E_2 E_1}\right)\left(\frac{I_1 I_2}{I_2 I_1}\right)\left(\frac{\Delta_{1a}\Delta_{2b}}{\Delta_{2a}\Delta_{1b}}\right)^{-m} exp\left(\frac{\pi f(\Delta_{2a} - \Delta_{1a} + \Delta_{1b} - \Delta_{2b})}{v_{Lg}Q(f)}\right) \quad (9)$$

as presented by Bao et al. (2011), with all the notations being the same as those defined in section 4.1. As explained in the previous section, instrumental responses are removed during the data processing. In equation (9), the site response terms can also be eliminated, resulting in the form:

$$\frac{1}{Q(f)} = \frac{v_{Lg}}{\pi f(\Delta_{2a} - \Delta_{1a} - \Delta_{2b} + \Delta_{1b})}\ln\left[\frac{A_{1a}A_{2b}}{A_{2a}A_{1b}}\left(\frac{\Delta_{1a}\Delta_{2b}}{\Delta_{2a}\Delta_{1b}}\right)^m\right]. \quad (10)$$

From equation (10), we can see that the RSTM can effectively remove the source and site effects. However, its complex geometry significantly lessens the number of possible pairs, consequently limiting spatial data coverage. Thus, in this study, we use the RSTM only for measuring the relative site responses rather than estimating the *Lg Q*.

By combining equation (8) and (10), we reach equation (11):

$$\frac{A_{1a}A_{1b}}{A_{2a}A_{2b}}$$

$$= \left(\frac{E_1 I_1}{E_2 I_2}\right)^2 \left(\frac{\Delta_{1a}\Delta_{1b}}{\Delta_{2a}\Delta_{2b}}\right)^{-m} \left[\frac{A_{1a}A_{2b}}{A_{2a}A_{1b}}\left(\frac{\Delta_{1a}\Delta_{2b}}{\Delta_{2a}\Delta_{1b}}\right)^m\right]^{\frac{\Delta_{2a}-\Delta_{1a}+\Delta_{2b}-\Delta_{1b}}{\Delta_{2a}-\Delta_{1a}-\Delta_{2b}+\Delta_{1b}}}. \quad (11)$$

Therefore, the relative site responses can be obtained by a following relationship:

$$\ln\left(\frac{E_1}{E_2}\right) = \frac{\Delta_{1b} - \Delta_{2b}}{\Delta_{2a} - \Delta_{1a} - \Delta_{2b} + \Delta_{1b}} \ln\left(\frac{A_{1a}\Delta_{1a}^m}{A_{2a}\Delta_{2a}^m}\right)$$

$$+ \frac{\Delta_{2a} - \Delta_{1a}}{\Delta_{2a} - \Delta_{1a} - \Delta_{2b} + \Delta_{1b}} \ln\left(\frac{A_{1b}\Delta_{1b}^m}{A_{2b}\Delta_{2b}^m}\right). \tag{12}$$

Equation (12) can also be represented by a linear system $\mathbf{f} = \mathbf{Hk}$, where the column vector $\mathbf{f}$ corresponds to the right-hand side of the equation (12) for all possible RSTM pairs and the vector $\mathbf{k}$ being the desired log site responses. A sparse matrix $\mathbf{H}$ represents the coefficients of the two log site terms in the left-hand side of the equation:

$$\mathbf{H} = \begin{bmatrix} 1 & -1 & 0 & & 0 & 0 \\ 1 & 0 & -1 & \cdots & 0 & 0 \\ 0 & 1 & -1 & & 0 & 0 \\ & \vdots & & \ddots & \vdots & \\ 0 & 0 & 0 & \cdots & 1 & -1 \end{bmatrix}. \tag{13}$$

If there are more than one observation for a two-station pair, we used the mean of all observed $\mathbf{f}$ values for the pair. In actual calculation, matrix $\mathbf{H}$ often becomes singular when station coverage is highly limited. In order to prevent the $\mathbf{H}$ from being singular, we used a small quantity ε of 1e-15 instead of 0 when constructing the matrix.

Since the method only estimates the relative difference between the stations, the RTSM cannot resolve for an absolute site response. Rather, it gives site response estimates relative to several reference stations. The site response values at the selected reference stations are often assumed to be zero in log10 scale, representing neither amplification nor de-amplification at the reference stations. With the assumption, rows are appended to the $\mathbf{f}$ and $\mathbf{H}$ by the number of reference stations. Extended rows have a value of the ε for the $\mathbf{f}$ representing zero site response, and additional rows in the $\mathbf{H}$ have a value of 1 for a column representing the reference station, and otherwise, ε. Gallegos et al. (2017) suggested that utilizing more than a

single station as reference station is likely to ensure more reliable solution since multiple references help stabilizing the inversion. Then, the system is inverted via the same method as inverting the *Lg Q*.

When constructing a two-station-two-event pair, we can consider four possible cases (Fig. 8). The first case represents a geometry where two events are positioned on either side of the stations (Fig. 8a), while both events lie outside the station pair on the same side, in the second case (Fig. 8b). In the third case, one of the events is located between the two stations, while the other is outside the station pair (Fig. 8c). The last case, also known as the reverse two-event method (RTEM), assumes both events to be situated between the station pair (Fig. 8d). A physical meaning of the denominator of the coefficients, $\Delta_{2a} - \Delta_{1a} - \Delta_{2b} + \Delta_{1b}$, in the equation (12) is the difference in the interstation distance for event *a* and *b*, respectively (Chun et al., 1987). However, since the setting in case 3 and 4 lacks the physical meaning, we exclude the two cases. In the second case, interstation distance from event *a* (i.e., $\Delta_{1a} - \Delta_{2a}$) approximates that from event *b* (i.e., $\Delta_{1b} - \Delta_{2b}$). The proximity gives rise to an unexpectedly large **f** value since the denominator is close to 0. In contrast, interstation distances from both events are approximately the same in magnitude, with opposite sign. This leads the coefficients being equally 1/2, which greatly stabilizes the f value estimation. Therefore, we used RTSM pairs that strictly follow case 1 geometry. Along with the geometry control, we limited the azimuthal and back azimuthal differences from both events to be less than 15°, in order to maintain the linearity assumption.

Figure 6. Event-station geometries for TSM and RTSM. Examples showing (a) an ideal geometry for the TSM, and more realistic geometries for (b) TSM and (c) RTSM. The azimuthal difference and back azimuthal difference are regulated to be smaller than 15° for both TSM and RTSM.

(a) Ideal TSM   **(b) Realistic TSM**   **(c) RTSM**
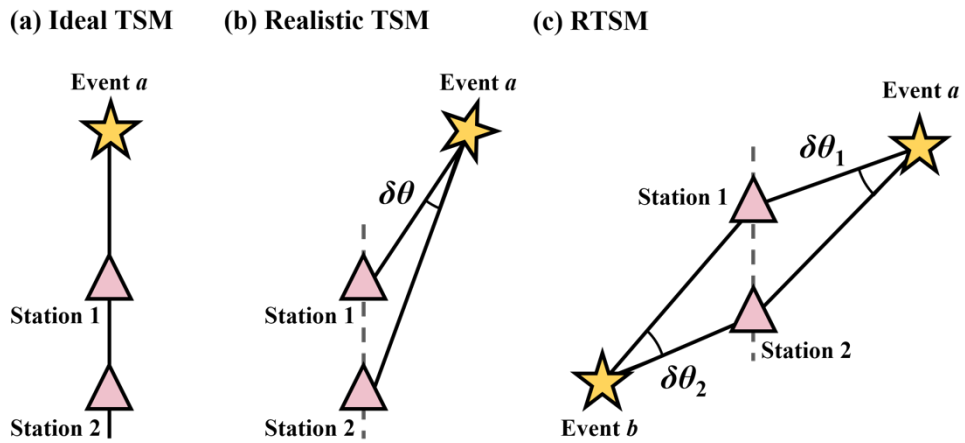
Figure 7. Example of cell grids and two-station pairs along the profile A–A'. Height and width of the cell are 0.1° and ~0.2°, respectively. Black triangles represent location of the CCSE array and violet triangles indicate GSN stations. Sample event for this figure is same with that shown in Fig. 3.
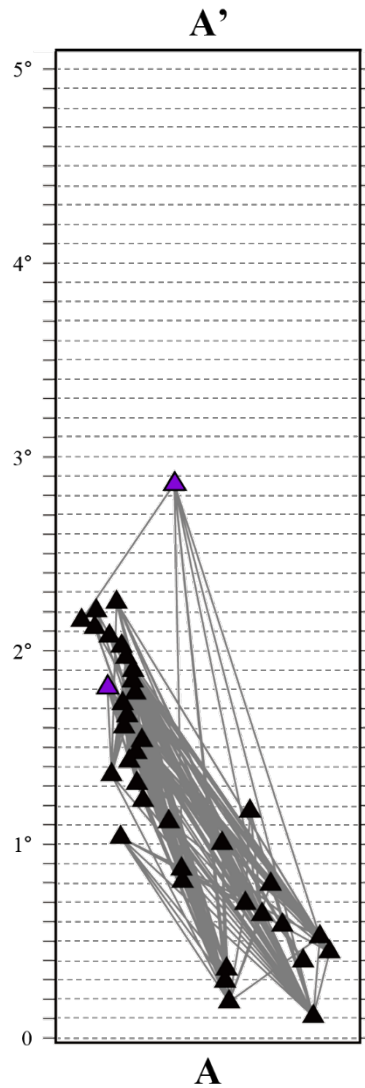
Figure 8. Four possible station-event geometries of the RTSM. (a) Case 1 represents a geometry when both events are outside the two stations, at either side of the station. (b) Case 2 assumes when both events are outside the two stations, but at the same side of the stations. (c) Case 3 describes a situation when one event sits between the two-station pairs while the other is outside of the pairs. (d) Case 4, also known as the RTEM geometry, represents a geometry when both stations lie within the two-station pair.
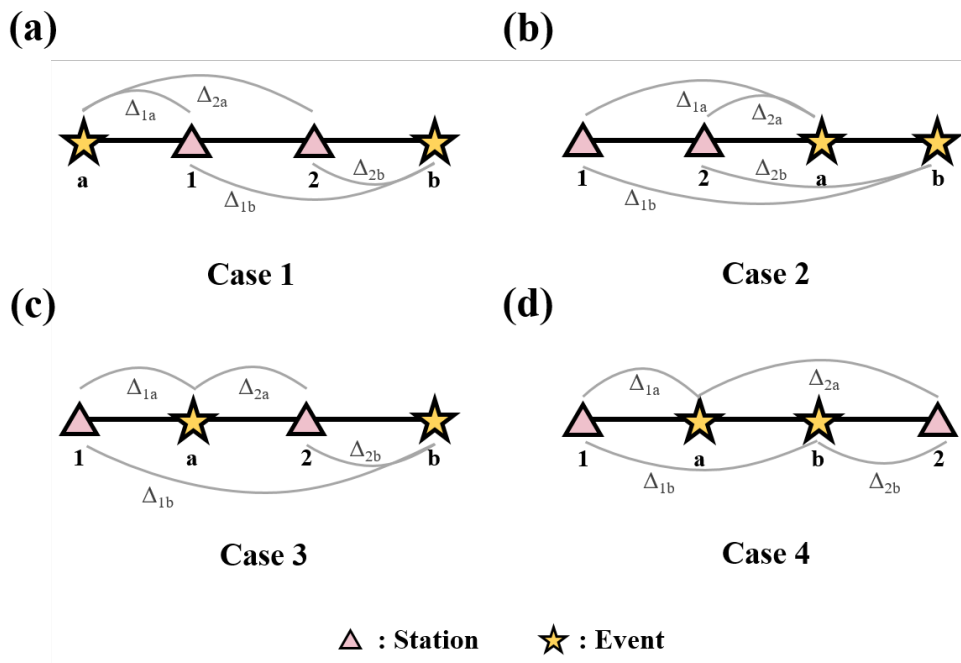
Chapter 5

Results

5.1. 1-D Checker-board Resolution Test

To check the resolution of the inversion result, we performed a 1-D checker-board resolution test. We used an alternating Q model centering at 150 with ±20 per cent perturbations for each cell (Fig. 9). Based on the model, synthetic interstation Q data are generated with ±10 per cent random noise, using the TSM. Since the TSM is sensitive to the input data, 10 per cent of random noise results in a slight fluctuation when retrieving the input perturbation. We repeated the test for 100 times to compensate for the fluctuation. We observed that whenever the grid size is inappropriate, not only the mean Q structure highly deviates from the input but also the level of fluctuation becomes severe. Thus, we determined the grid size considering both the mean of retrieved Q values and the extent of fluctuation.

As briefly mentioned in section 3, incorporation of the GSN stations gives rise to a discrepancy in the station density: the average interstation distance within

the CCSE array is ~6.5 km whereas it is ~23.7 km outside the array. Due to this inconsistency, selection of a uniform cell size resulted in a poor resolution for the regions farther than 250 km, the easternmost point of the CCSE array (Fig. 9a). Thus, we used a cell size of 0.3° for the first 250 km region covered by the CCSE and a larger cell size of 0.9° for the farther region covered by the GSN. Adopting the varying cell size allowed us to better resolve both regions (Fig. 9b).

5.2. Relative Site Response Result

As explained in section 4.2., selecting an appropriate set of reference stations is critical in relative site response measurement. To understand the effect of the choice of reference stations, we adopted several sets of reference stations and compared the result (Fig. 10). Figure 10a shows the pattern of site responses when choosing each station, from CC01 to RVFF, as reference and we found that only the level of amplitudes changed while their trends were mostly consistent. The change in amplitudes seems reasonable since we are measuring relative values to the reference. Similar results are obtained when selecting more than two stations as reference. We randomly picked two stations as reference (Table 3), estimated the relative site response with respect to the reference and repeated the whole process for 25 times (Fig. 10b). The distribution of the site response appears to be robust regardless of the reference stations, and we confirm that the selection of reference station does not affect the pattern of site response. In terms of the amplitude, it is recommended to select stations above the general rock sites as reference stations since the references

31

are assumed to be free from both amplification and de-amplification. Thus, we selected station CC03 and CC38, that are closest to the rock site, as the reference stations, based on the National Earthquake Hazards Reduction Program (NEHRP) site classification (Table 4). Note that the terms 'amplification' and 'de-amplification' used for the rest of this paper are relative to the two reference stations, and might not always indicate amplification or de-amplification in absolute sense.

Relative site responses for four center frequencies 0.75 Hz, 1 Hz, 2 Hz, and 2.75 Hz, are obtained using the RTSM (Fig. 11). At all frequencies, positive relative site response values (i.e., amplification) are obtained from most of the stations, reflecting pervasive sedimentary rocks present at the surface of the region. Also, the site response estimates generally increase as the frequency increases. At 0.75 Hz and 1 Hz, site responses show a similar pattern. Strong positive site responses (~1.0) are observed in the regions filled with unconsolidated or loosely consolidated sedimentary deposits, such as the Central Valley. Weak negative values (~ -0.1; i.e., de-amplification) are obtained at the western edge of the basin (e.g., CC15). At higher frequencies (2 Hz and 2.75 Hz), both amplification and de-amplification become more significant that in the lower frequencies. Stronger positive site responses (> 1.5) are observed in sedimentary regions. At the westernmost part of the CV, weak (~ -0.1) and moderate (~ -0.5) negative site responses are obtained for 2 Hz and 2.75 Hz, respectively. At all frequencies, weak positive values (< 0.5) are observed at the eastern end of the CCSE array, where it begins to meet the Sierra Nevada mountain range.

5.3. Lateral Variation of *Lg Q*

5.3.1. TSM Results

We first obtained lateral variation of *Lg Q* along a great circle profile (A–A') along the CCSE array, using the conventional TSM (Fig. 12a). The inversion results are obtained after 31 – 44 iterations, with variance reductions ranging from 65.24% to 79.81% (Table 5) at each frequency. *Lg Q* estimates tend to increase as the frequency increases, average Q value rising from 60.31 at 0.75 Hz to 147.97 at 2.75 Hz. Similar *Lg Q* distribution is observed at all frequencies, with about four high-Q peaks along the profile. For the convenience, we shall use the term 'uncorrected' for the rest of the thesis to refer to the result obtained by the conventional TSM.

As delineated in section 4.1., we corrected the Q estimates for the site response term, reported in the previous section (Fig. 12b). The number of iterations slightly decreased to 15 – 25 compared to the uncorrected result, with variance reductions of 74.08% – 78.79% (Table 6). After the correction, average Q value slightly increased at all frequencies and a rise in the *Lg Q* value with greater distance from the coast becomes more remarkable. This gentle increment might reflect the change in the stiffness of the rocks, from the soft marine accretionary wedges (Blake et al., 1988) to the stiff granitic intrusions (Godfrey and Klemperer, 1998). Similar to the uncorrected result, the *Lg Q* values increase as the center frequency increases. However, unlike the uncorrected result, the location of notable peaks is not consistent at the four frequencies. The peak location is similar for the lower frequencies (0.75 Hz and 1 Hz), being at ~150 km, 250 km and 417 km east from the point A, while

33

the peaks lie at ~217 km and 317 km from the point at 2.75 Hz. An intermediate behavior is obtained at 2 Hz, presenting a peak at ~217 km following the pattern at 2.75 Hz, while a gentle increase is observed after ~250 km from the point A rather than striking peaks as in the case of lower and higher frequencies.

5.3.2. Passband Effect

To examine the effect of the passband of the filter, we set several bandwidths and compared the results at 1 Hz (Fig. 13). We postulated two broader passbands of 0.1 – 4.0 Hz (i.e., He et al., 2017) and 0.25 – 1.75 Hz, and one narrower passband of 0.75 – 1.25 Hz (Table 7). For convenience, we denote the two broader passbands as 'very-wide' and 'moderately-wide', and the narrower passband as 'narrow'. We provide a 500 times bootstrapping uncertainty range in order to better examine the extent of deviation in Q caused by various passbands. With the conventional TSM, the results are consistent and they fall well within the range of bootstrapped uncertainty range of the current result (Fig. 13a). However, when we apply the site response correction, deviation from the current result becomes more evident (Fig. 13b), particularly for the very-wide case where the peaks are shifted (at ~187 km) and dissipated (at ~250 km). We consider that the discrepancy arises due to the sensitivity of the site-response-corrected result to the change in frequency, since the shifted peak location of ~ 183 km is between the first peak observed at 1 Hz (~150 km) and 2 Hz (~217 km), and the dissipated peak coincides with the location of the low-Q peak exhibited at the higher frequencies. We observe that adopting the moderately-wide bandwidth prevents the high-frequency properties being included

in the data. In this case, the estimated Q values also remain within the bootstrapped uncertainty range. For the narrow passband case, although the pattern of the peaks is generally preserved, the amplitude near 300 km slightly deviates from the bootstrapped uncertainty range and the first peak at ~ 150 km is not resolved. Based on this result, we infer that selecting a passband that is too wide or too narrow might be inappropriate for constraining the frequency-dependent behavior of the *Lg* wave attenuation. Thus, we suggest to choose a passband by adding 25 – 50 per cent of the center frequency.

Figure 9. One-dimensional checker-board resolution test result with (a) a uniform grid size of 0.3° and (b) a varying grid size of 0.3° to 0.9°. Black line signifies input Q structure with 20% perturbation and pink line indicates the average of the retrieved pattern. Grey shade represents the extent of fluctuation after 100 times of repeated test. Note that both mean Q values (pink lines) and the level of fluctuation (grey shades) are greatly improved when adopting the varying grid size.
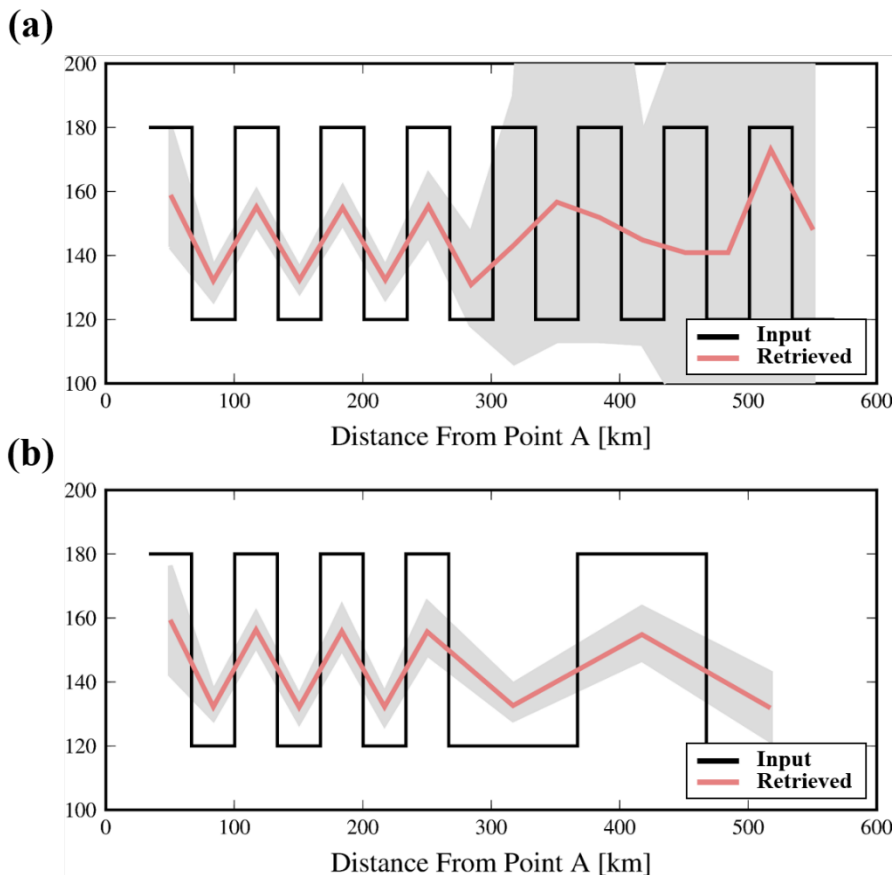
Figure 10. Sensitivity check for the relative site response to the selection of reference stations. (a) The pattern of relative site responses when choosing each station, from CC01 to RVFF, as reference. Light-blue vertical lines indicate the location of each station chosen as reference and black solid lines connect relative site response value at each station for each case. (b) The pattern of relative site responses when choosing two random stations as reference and repeating for 25 times. Color scale denotes trial number and the two-station set used for each trial is listed in Table 3.
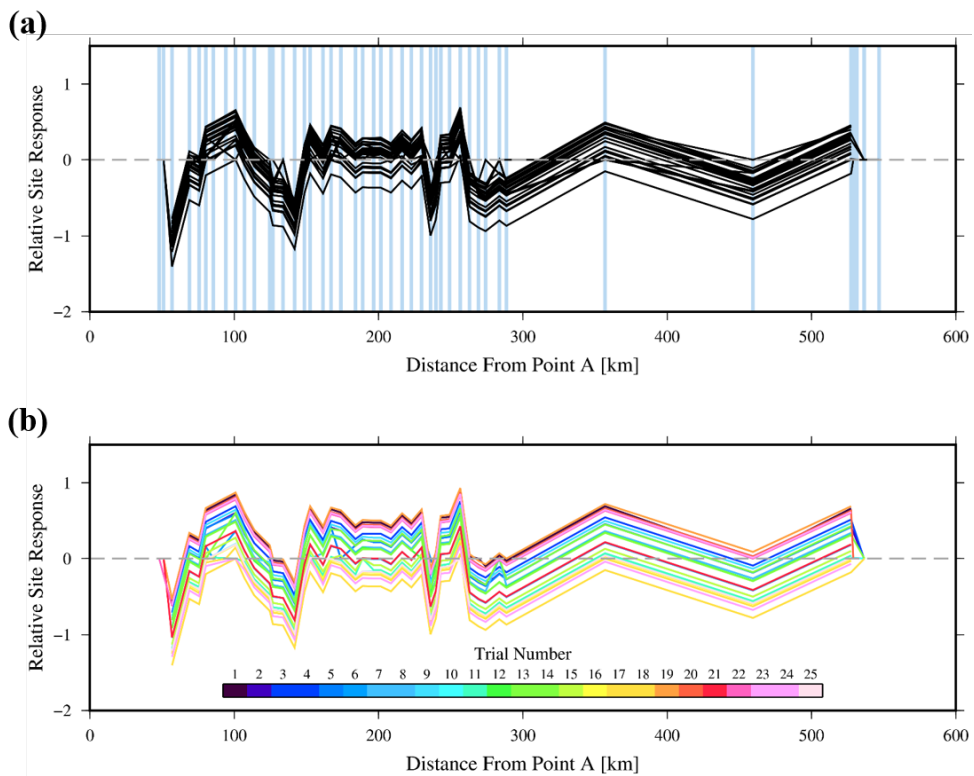
Figure 11. Relative site responses centering at four frequencies and its comparison to the thickness of the sediments (Mooney and Kaban, 2010). CC03 and CC38 are used as reference stations as indicated in the figure. Site response of most of the stations exhibits positive value, indicating the soft surficial geology at the region. Stronger amplification is observed at younger sedimentary region including the CV while weak to moderate de-amplification is observed at the east of the SAF.
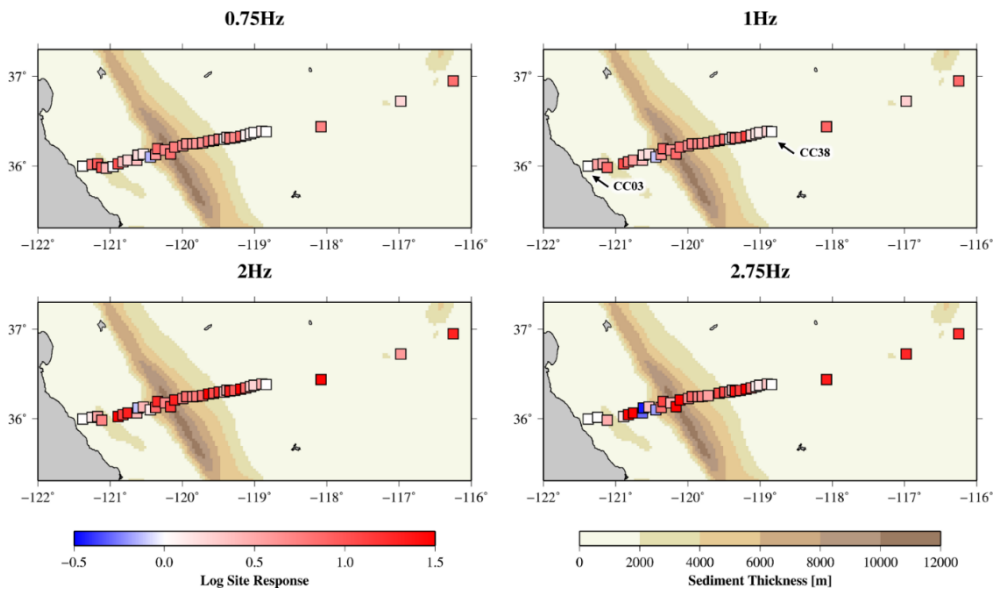
Figure 12. Lateral variation of *Lg Q* along A − A' profile. (a) Conventional TSM result. (b) The site-response-corrected result. Above the *Lg Q* variation plot, the distribution of the sediment thickness (Mooney and Kaban, 2010) and the topography (GMRT; Ryan et al., 2009) along the profile are shown. Grey shades denote the inversion grids. Note for the considerable change in the peak location after the correction.
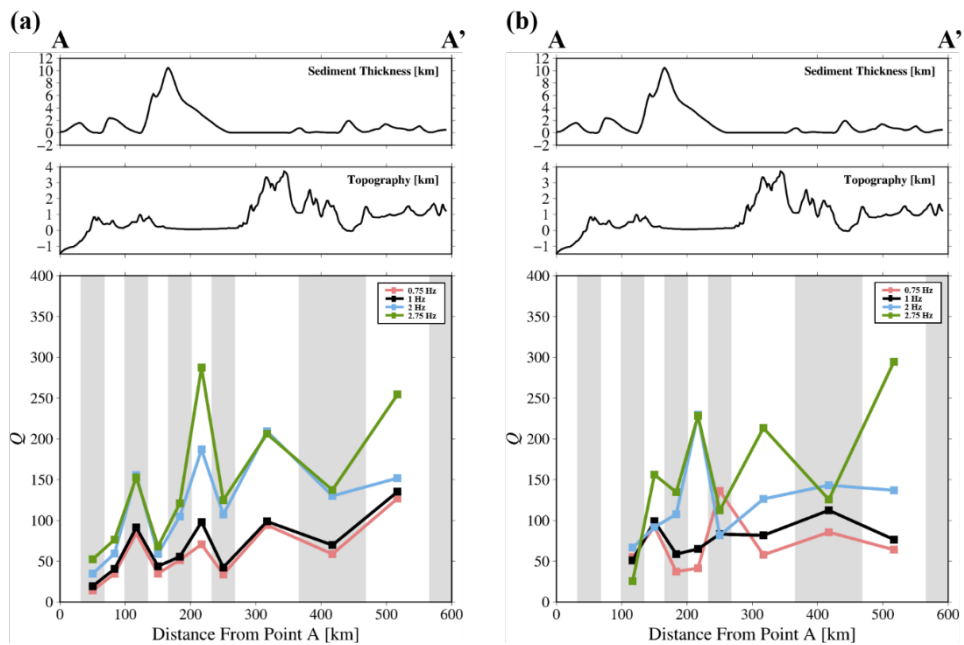
Figure 13. Comparison of results obtained by using four different passbands centering at 1 Hz. (a) Results using the conventional TSM and (b) the site-response corrected TSM. Specific band-pass is described in Table 6. Grey shade represents the 500 times bootstrapped uncertainty range obtained from the current passband. Note that the general pattern and peak locations are consistent for the moderately-wide and narrow bandwidths, while the position and the amplitude of the peaks are changed for the very-wide case. Before ~300 km, the amplitude lies well within the range of the bootstrapped uncertainties for the moderately-wide and narrow bandwidth cases.
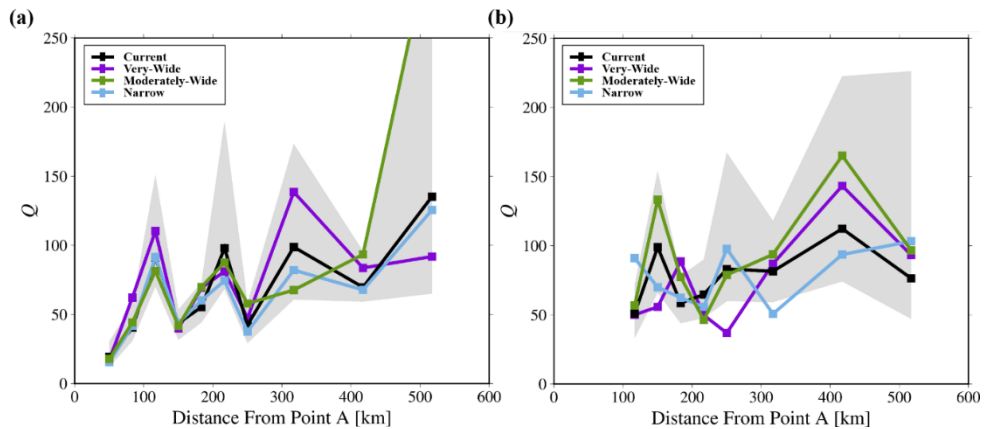
Table 3. List of reference station pairs used for the estimation of the relative site responses in Figure 10.

Trial number	Network	Station	Distance from point A (km)	Network	Station	Distance from point A(km)
1	TO	CC34	269.14	SN	HEL	459.37
2	TO	CC05	75.84	SN	RVSE	536.17
3	TO	CC12	124.74	SN	RVSE	536.17
4	TO	CC33	263.15	TO	CC33	263.15
5	TO	CC20	173.78	TO	CC29	235.93
6	TO	CC07	85.55	TO	CC22	189.04
7	TO	CC19	167.11	TO	CC22	189.04
8	TO	CC17	152.57	TO	CC37	283.65
9	TO	CC11	113.72	CI	VOG	239.78
10	TO	CC19	167.11	SN	RVNE	536.57
11	TO	CC09	100.94	TO	CC22	189.04
12	TO	CC28	229.91	CI	VOG	239.78
13	TO	CC11	113.72	SN	RVNE	536.57
14	TO	CC06	80.22	TO	CC37	283.65
15	TO	CC19	167.11	TO	CC22	189.04
16	TO	CC17	152.57	TO	CC17	152.57
17	TO	CC08	94.08	CI	CWC	356.94
18	TO	CC09	100.94	SN	RVNE	536.57
19	TO	CC02	51.03	TO	CC38	288.68
20	TO	CC33	263.15	SN	SPRS	529.01
21	TO	CC02	51.03	TO	CC23	196.65
22	TO	CC01	48.04	SN	HEL	459.37
23	CI	VOG	239.78	TO	CC37	283.65
24	TO	CC09	100.94	TO	CC17	152.57
25	TO	CC18	161.4	TO	CC32	256.66

Table 4. National Earthquake Hazards Reduction Program (NEHRP) site classification based on the shallow shear-wave velocity (V_{S30}).

Site Class	Description	V_{S30} (m/s)
A	Hard Rock	> 1500
B	Rock	760 – 1500
C	Very Dense Soil and Soft Rock	360 – 760
D	Stiff Soil	180 – 360
E	Soft Soil	< 180

Table 5. Summary of the inversion result with the conventional TSM. Variance reduction (VR), root-mean-square error (RMSE), the number of iteration to the solution and the mean Q value at each frequency are presented.

Frequency (Hz)	VR (%)	RMSE	# It. (times)	Mean Q
0.75	79.81	1.23	44	60.31
1	79.46	1.00	34	69.41
2	72.98	0.75	31	119.83
2.75	65.24	0.77	32	147.97

Table 6. Summary of the inversion result with the site-response-corrected TSM. Variance reduction (VR), root-mean-square error (RMSE), the number of iteration to the solution and the mean Q value at each frequency are presented.

Frequency (Hz)	VR (%)	RMSE	# It. (times)	Mean Q
0.75	78.79	1.00	20	71.16
1	78.16	0.80	15	78.34
2	74.08	0.60	25	122.90
2.75	74.37	0.67	25	161.27

Table 7. The lower- and upper limits of the passband used for the four cases.

Trial Name	Lower (Hz)	Upper (Hz)	Center (Hz)
Current[*]	0.5	1.5	1
Very-Wide[**]	0.1	4.0	1
Moderately-Wide	0.25	1.75	1
Narrow	0.75	1.25	1

[*] Gallegos et al. (2017), Chen & Xie (2017), Ranasinghe et al. (2018)
[**] He et al. (2017)

Chapter 6

Discussion

6.1. Site Response

As shown in section 5.2., two notable features in the site response estimates are enhanced degree of amplification in the sedimentary regions and moderate de-amplification near the SAF. Regarding the amplification, we found that although the level of amplification is affected by the thickness of sediments to some extent, a linear relationship between the two is very weak. Rather, degree of consolidation and surface lithology can play more significant role in determining the level of amplification. Most of the stations that show strong amplification lies upon the Pleistocene-Holocene sedimentary rocks which are unconsolidated or semi-consolidated. In contrast, weak amplification is observed at either well consolidated sedimentary regions or the regions with older lithology, mostly being Mesozoic. The other notable feature, the de-amplification at the western edge of the basin, might also be attributed to the old and solid lithology distributed near the fault zone. The

strong relation to the surface lithology generally agrees with the observation that the site response is mostly affected by the shallow surface geology (Borcherdt, 1970; Borcherdt and Gibbs, 1976; Rogers et al., 1979; Su et al., 1992). Also, our observation that the geologic age considerably affects the level of amplification strengthens previous reports on the relation between the age of a rock and the level of site amplification (Su et al., 1992).

To examine the relationship between the site response and surface geology, we compared our result to the V_{S30} data (Fig. 14a; Worden et al., 2015), a shear-wave velocity in the upper 30 m depth. The result is shown in Figure 14b, where a strong negative correlation with the V_{S30} distribution is observed at all frequencies, with high coefficient of determination (> 0.7) and small p-values (< 0.05). The result is in good agreement with previously reported values (Yassminh et al., 2019), supporting our observation that the site responses tend to be larger at soft, low-velocity regions. However, we do not observe any relationship to the topography from the result. We suspect that it might be attributed to the low resolution at Sierra Nevada, where only the sparse GSN stations are available. On the other hand, the topography simply might not be a significant factor for determining the site response at the region.

6.2. Frequency Dependence of *Lg Q*

For the site-response-corrected result, we investigated the frequency dependence of the *Lg Q* values at the region. We averaged the *Q* values at each frequency (Table 8), and obtained a best-fitting curve for the mean *Q* values (Fig. 15). As a result, we

obtained a power-law frequency dependence of $Q(f) = (81 \pm 8)f^{(0.62 \pm 0.11)}$, which lies in the lowermost range of the previous estimates of $\sim 80 - 300$, conducted in the western US (Singh and Hermann, 1983; Baqer and Mitchell, 1998; Phillips and Stead, 2008; Gallegos et al., 2017). Such low value of $\sim 81 \pm 8$ might reflect the existence of massive unconsolidated sedimentary deposits and presence of fluids in the upper crust that has been formed through past crustal and mantle heating, as suggested by Baqer and Mithcell (1998). The frequency dependence factor of 0.62 ± 0.11 is in a good agreement with the previously reported values ($0.25 - 0.72$; Singh and Hermann, 1983; Baqer and Mitchell, 1998; Erickson et al., 2004; Benz et al., 1997; Gallegos et al., 2017), highlighting the strong tectonic activity of the region.

6.3. Relation to the Regional Geology

In this section, we compare our result to the regional geological properties in order to understand the effect of each property to the *Lg Q* attenuation. *Lg Q* values are often correlated with several crustal characteristics such as thick sediments (Mitchell and Hwang, 1987; Wei et al., 2017; Zhao and Mousavi, 2018), thermal conditions (Frankel, 1991), shear-wave velocity (Gallegos et al., 2017; Zhao and Mousavi, 2018), crustal thickness (Zhao et al., 2010; Zhao et al., 2013a) or partial melting in the crust (Xie et al., 2004). Here, we focus on the relationship with the sediments, shear-wave velocity structure and Moho temperature.

First of all, we discuss the discrepancy between the uncorrected and corrected result near the CV (Fig. 12). Before correction, we observe a locally low *Q* value of

~50 between 100 – 200 km east from the point A. In contrast, a locally high Q value of ~100 at the same spot is observed after the correction. We consider the cause of the discrepancy is the removal of surficial effects resulting from the site response correction. Since the Lg wave can be modeled as a crustal guide wave, $Lg\ Q$ represents the crustal averaged attenuation structure (Xie et al., 2004). By the correction of site terms, the effect of sediments at the surface, a major contributor to the Lg attenuation, is minimized so that the effect of deeper structure could be revealed. When comparing the results before and after the correction at higher frequencies, we found that the general trend in the high-frequency results did not change as severely as the lower frequency results. Since higher frequencies are highly sensitive to shallower structures (Wei et al., 2017), the effect of site response correction is less critical at higher frequencies than at the lower frequencies.

The depth sensitivity of the result can also be observed by the comparison to the shear-wave velocity (Fig. 16a, b, e). In central California, a strong contrast in shallow and deep shear-wave velocity has been reported by several previous studies (Shen et al., 2013; Jiang et al., 2018), particularly beneath the CV. According to the estimates provided by Shen et al. (2013), the V_S at the center of the CV varies from ~1.4 km s^{-1} near the surface to ~3.9 km s^{-1} near the Moho (Fig. 16a-b). The extremely low shear-wave velocity near the surface of the valley can be mainly attributed to the thick sediments, most of which are not fully consolidated. The origin of the imaged high velocity structure beneath the CV is still under debate: it is often interpreted as a remnant of an underthrusted oceanic lithosphere (Wang et al., 2013) or as a relic of an ancient craton (Shen et al., 2013) whereas Godfrey and Klemperer (1998) and Fliedner et al. (2000) considered it as an extension of the great valley ophiolite. Moreover, based on their spatial correlation, we also note for the possible

49

connection between the high-V_S structure at the lower crust and the Isabella anomaly, as suggested by Jiang et al. (2018). The shear-wave velocity structure is well known to have a positive correlation with Lg Q patterns. Thus, we compared the shallow (upper 3 km) and deep (15 km to a depth of Moho) shear-wave structure provided by Shen et al. (2013) to our site-response-corrected Lg Q result at each frequency (Fig. 16e). As a result, we observed that the pattern at lower frequencies (0.75 Hz and 1 Hz) seem to resemble some notable changes in the deep V_S structure (red circles of Fig. 16), while the shallower V_S structure seems to be imaged by higher frequencies (blue circles of Fig. 16).

In addition, we examined the relation of Moho temperature (Fig. 16c; Schutt et al., 2018) and Pn velocity structure (Fig. 16d; Buehler and Shearer, 2017) to our Lg Q estimates. Along the A – A' profile, the Moho temperature gradually increases from the coast to a distance of ~300 km and then gently decreases as moving further inland. The Pn velocity structure shows a reversed relationship to the Moho temperature variation as it mostly travels along the crust-mantle boundary, being affected by the properties of the Moho (Schutt et al., 2018). An inversely proportional relationship between the temperature and the Lg Q values is generally expected considering the strong attenuation of the Lg wave caused by the high temperature (Frankel, 1991; Wei et al., 2017). At 0.75 Hz, a distinct low-Q peak is imaged at the point of the maximum Moho temperature and minimum Pn velocity, while the peak is still observable at 1 Hz but not as much striking as at 0.75 Hz. Contrastingly, the effect of Moho temperature seems to be insignificant at higher frequencies, with no clear peak at 2 Hz or even with a high-Q peak at 2.75 Hz.

From the comparison, we found a consistent relationship of deeper geologic structure to the Lg Q estimates at lower frequency, and vice versa. Therefore, we

suggest that the correction is indeed effective for removing the surficial properties. However, approximate depth resolution for each frequency is still unclear.

6.4. Comparison to the Sacramento Valley Region

To examine whether the scope of our result is only local or can be applicable to other regions, we compared our result with an analogous region, the Sacramento Valley. The region is located about 2° north to the CCSE array, and also filled with thick sediments enclosed by the Sierra Nevada mountain range. However, the severe contrast in the deep and shallow shear-wave velocity is not observed below the Sacramento Valley (Fig. 17a-b).

The density of available stations in the Sacramento Valley is substantially low compared to that of the CCSE array, with average interstation distance being ~ 16.4 km at Sacramento Valley, while being ~ 6.5 km at the CCSE array. The deficiency in station density leads to the selection of a larger grid size of 0.9° for the first 200 km from the coast and a smaller cell size of 0.6° for farther eastern regions where data availability is better than the western coast. We investigated the spatial variation of the Lg Q along a profile B–B' (Fig. 1), approximately 2° north to the profile A–A'. The inversion stopped after 22 – 58 iterations, with variance reduction values ranging from 62.48% to 70.12% (Table 9). Station operation periods in the Sacramento Valley do not overlap sufficiently so that the total amount of available data is remarkably low at the region. Thus, we focus only on two distinct observations, change of pattern at ~100 km and the overall consistency before and

after the correction, and do not interpret each peak.

We find that the results are consistent before and after the correction except for the region of ~ 100 km from the point B, where a low Q values are observed before the correction (Fig. 17c, pink squares and lines) while local high-Q peak is imaged after the correction (Fig. 17c, black squares and lines). The inconsistency is particularly remarkable at lower frequencies (0.75 Hz and 1 Hz). When plotted with the sediment thickness, we can see that the point of inconsistency corresponds to the site of maximum sediment thickness. Based on the spatial correlation between the two, the notable change in the Q pattern after the correction seems to support the idea that the correction eliminates the surficial effects, as observed in the CCSE array. In contrast, we note a strong consistency in Lg Q patterns in proximity to the Sierra Nevada (> ~300 km from B). Near the mountain range, only the sparse GSN network stations are available for the A–A' profile. This leads to a reversal in ray hits at the region, A–A' profile being lower than at B–B'. Considering the higher resolution along the B–B', the consistency in Q patterns regardless of the correction obtained in the Sacramento Valley seems to challenge the reliability of the inconsistency observed along the A-A'. To better understand the effect of site response correction near the Sierra Nevada, denser array data is required.

(a) V$_{S30}$ Distribution [m/s]

(b)

0.75Hz

R^2 = 0.7607, p = 0.0235
y = -0.0014x + 0.9828

1Hz

R^2 = 0.7468, p = 0.0264
y = -0.0015x + 1.1090

2Hz

R^2 = 0.8039, p = 0.0155
y = -0.0022x + 1.6321

2.75Hz

R^2 = 0.7224, p = 0.0321
y = -0.0022x + 1.5887
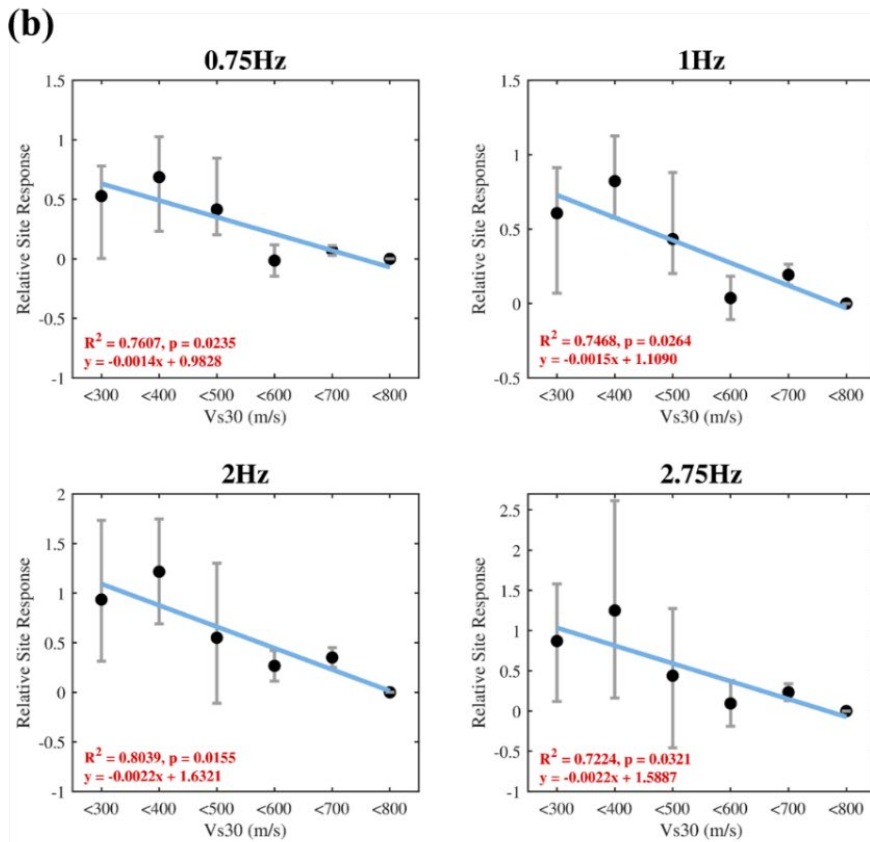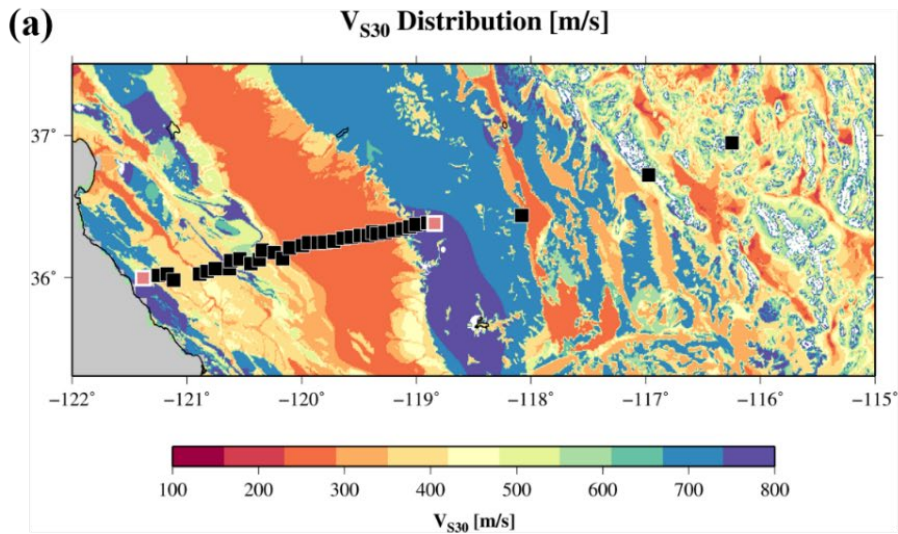
Figure 14. (Caption in next page)

Figure 14. Relative site response and its correlation to the V_{S30} structure. (a) A map view of V_{S30} distribution in the study area (Worden et al., 2015). Black squares represent the stations used in this study, and the pink squares indicate the reference stations (i.e., CC03 and CC38). (b) Correlation between the site response and interval-averaged V_{S30} structure. Grey bar indicates the range of true values in the interval. Square of the correlation coefficients (R^2), p-values and the relation are provided at the left bottom corner of each panel.

Figure 15. Frequency dependence estimation for the site-response corrected *Lg Q* values. Each point denotes the average *Q* value centering at the four frequencies, while the grey line denotes the best-fitting curve for the points. The power-law frequency dependence of *Q* estimates is provided at the right bottom corner of the plot.

Frequency Dependence

$$Q(f) = (81 \pm 8) f^{(0.62 \pm 0.11)}$$

(y-axis: log(Lg Q), x-axis: log(frequency))
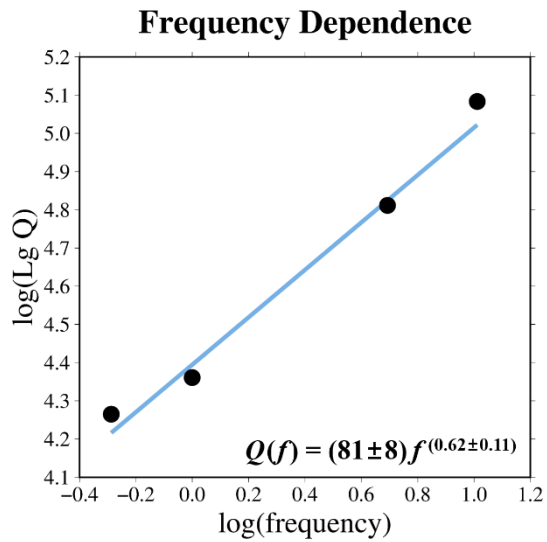
Figure 16. Lateral variation of the *Lg Q* and its comparison to other geologic properties. (a) Shallow- and (b) deep shear-wave velocity variation (Shen et al., 2013), (c) Moho temperature (Schutt et al., 2018) and (d) *Pn* velocity structure (Buehler and Shearer, 2017) along the profile A–A'. (e) Spatial variation of the site-response corrected *Lg Q* values. Grey shades represent the location and width of the inversion grid. Red circles denote the features related to the deep geology while the blue circles indicate the relation to the shallow structure. Note that the CV lies at ~ 150 km (3rd white cell) where a dramatic decrease in shallow shear-wave velocity is observed.
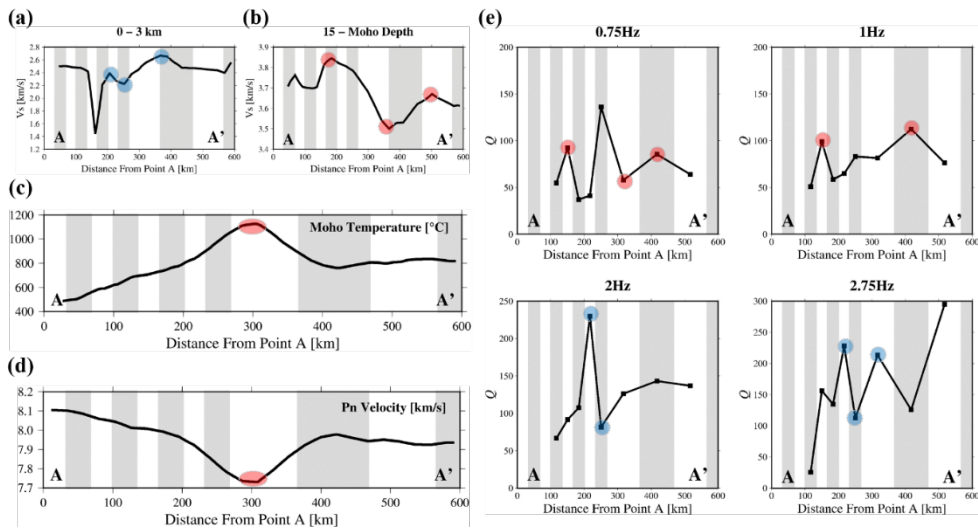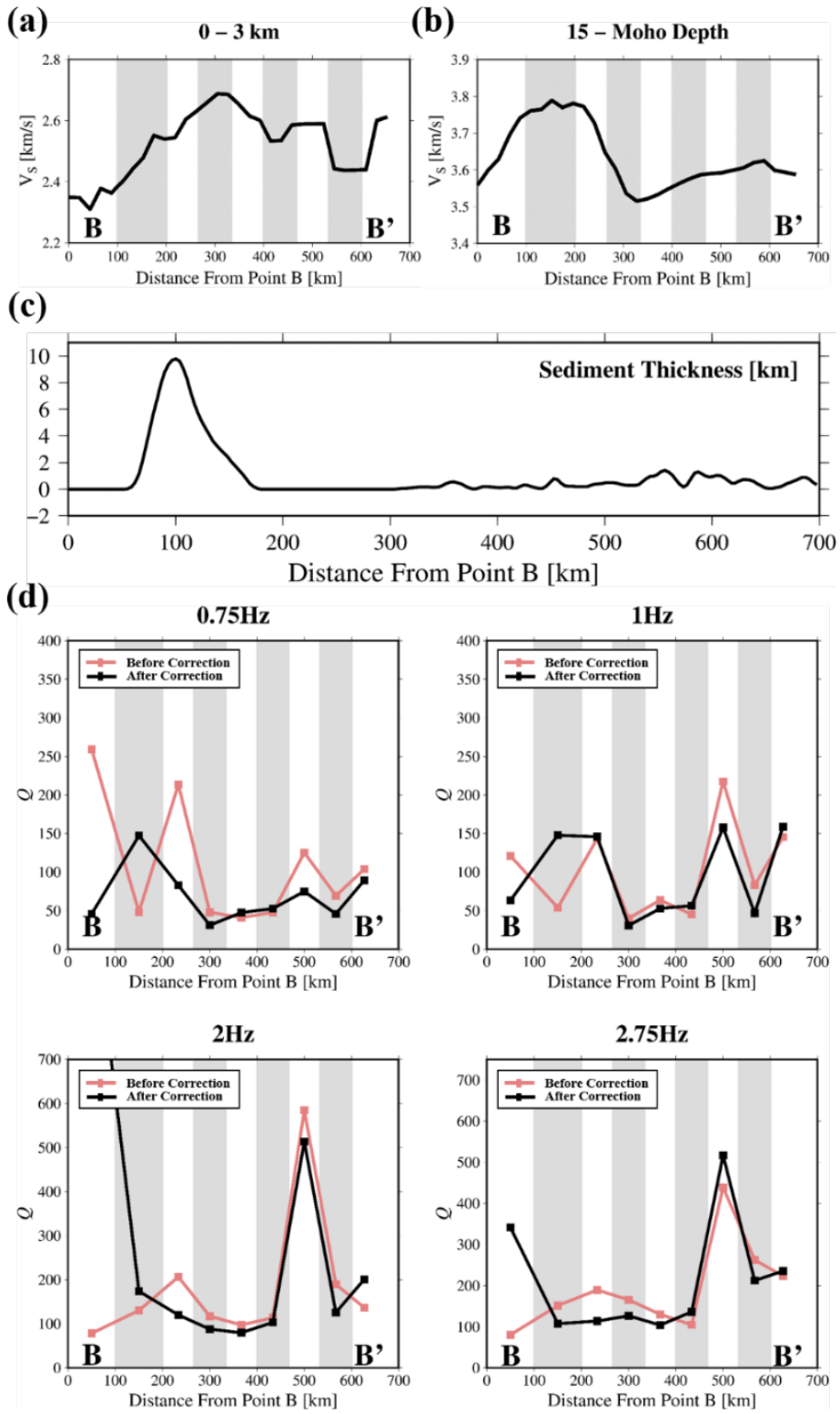
Figure 17. (Caption in next page)

Figure 17. *Lg Q* structure and its comparison to geologic properties at Sacramento Valley region. (a) Shallow- and (b) deep shear-wave velocity variation (Shen et al., 2013) and (c) sediment thickness (Mooney and Kaban, 2010) along the profile B–B'. (d) Spatial variation of the *Lg Q* values before (pink) and after (black) the site response correction. Note the value does not differ severely before and after the correction, except for ~100 km site, which coincides with the region of the maximum sediment thickness.

Table 8. Frequency dependence of the corrected result. Average Q value and corresponding 95% confidence interval are provided.

Frequency (Hz)	Average Q (95% confidence interval)
0.75	71.16 ($\pm$ 29.08)
1	78.34 ($\pm$ 18.34)
2	122.90 ($\pm$ 45.45)
2.75	161.27 ($\pm$ 73.86)

Table 9. Summary of the inversion result at Sacramento Valley, with the site-response-corrected TSM. Variance reduction (VR), root-mean-square error (RMSE), the number of iteration to the solution and the mean Q value at each frequency are presented.

Frequency (Hz)	VR (%)	RMSE	# It. (times)	Mean Q
0.75	65.96	2.51	25	68.52
1	64.93	2.16	22	95.53
2	70.12	0.94	58	275.23
2.75	70.22	0.72	49	210.31

Chapter 7

Conclusions

Using the data from the 37 quasi-linear CCSE array stations and 9 GSN stations, we estimated lateral variation of the *Lg Q* and relative site responses at four center frequencies, 0.75 Hz, 1 Hz, 2 Hz and 2.75 Hz, based on the TSM and RTSM, respectively. Most of the stations showed positive site responses, reflecting the widespread sedimentary rocks along the profile. We observed that the relative site responses exhibit a higher association to the age or consolidation status of the surface lithology, rather than the thickness of sediments. Furthermore, we found that the site responses are strongly correlated to the surficial shear-wave velocity (V_{S30}), supporting the intimate connection between the site terms and the surface geology.

We adopted the site responses to estimate *Lg Q* structure, and compared the result with conventional TSM. The correction resulted in the shift of the peak locations at lower frequencies (0.75 Hz and 1 Hz) while the effect of the correction

was trivial at higher frequencies (2 Hz and 2.75 Hz). Regardless of the center frequency, the *Lg Q* values increased from the western coast to the inland, reflecting the change in regional lithology. The site-response corrected *Lg Q* values tend to increase as the center frequency increases, following a power-law frequency dependence of $Q(f) = (81 \pm 8)f^{(0.62 \pm 0.11)}$. The estimate falls in a lowest range of the previously reported values, but such low value reflects the high tectonic activity and the presence of fluids in the region.

The spatial variation of the site-response-corrected *Lg Q* is compared to the sediment thickness, the shear-wave velocity and the Moho temperature. The low *Q* values often caused by thick sediments are missing, particularly at lower frequencies (0.75 Hz and 1 Hz). The deep and shallow shear-wave velocity seems to be correlated with the *Lg Q* structures at lower and higher frequencies, respectively, while the Moho temperature is correlated only to the lower frequency results. Thus, we confirmed that the correction reinforces the linkage of the *Lg Q* structure to the crustal average properties. Moreover, the lower frequencies are more prone to reflect deeper structures whereas the higher frequencies represent shallower geologic properties.

Finally, we compared our result to an analogous region, the Sacramento Valley. At the sedimentary basin, we obtained the reversal of the peak following the correction which strengthens our observation from the CCSE array. However, the correction did not yield in a notable change in the pattern of *Lg Q* values near the Sierra Nevada, which is in conflict with the result along the A-A' profile. This different behavior emphasizes a necessity of further investigation in the region with denser seismic networks.

References

Bao, X., Sandvol, E., Ni, J., Hearn, T., Chen, Y. J., & Shen, Y. (2011). High resolution regional seismic attenuation tomography in eastern Tibetan Plateau and adjacent regions. *Geophysical Research Letters*, 38(16).

Baqer, S., & Mitchell, B. J. (1998). Regional variation of Lg coda Q in the continental United States and its relation to crustal structure and evolution. In *Q of the Earth: Global, Regional, and Laboratory Studies* (pp. 613-638). Birkhäuser, Basel.

Becken, M., Ritter, O., Park, S. K., Bedrosian, P. A., Weckmann, U., & Weber, M. (2008). A deep crustal fluid channel into the San Andreas Fault system near Parkfield, California. *Geophysical Journal International*, 173(2), 718-732.

Bennington, N., Thurber, C., & Roecker, S. (2008). Three-dimensional seismic attenuation structure around the SAFOD site, Parkfield, California. *Bulletin of the Seismological Society of America*, *98*(6), 2934-2947.

Benz, H. M., Frankel, A., & Boore, D. M. (1997). Regional Lg attenuation for the continental United States. *Bulletin of the Seismological Society of*

America, *87*(3), 606-619.

Blandford, R. R. (1981). Seismic discrimination problems at regional distances. In *Identification of Seismic Sources—Earthquake or Underground Explosion* (pp. 695-740). Springer, Dordrecht.

Blake Jr, M. C. (1988). Metamorphic and tectonic evolution of the Franciscan Complex, northern California. *Metamorphism and crustal evolution of the Western United States*, 1035-1060.

Borcherdt, R. D. (1970). Effects of local geology on ground motion near San Francisco Bay. *Bulletin of the Seismological Society of America*, 60(1), 29-61.

Borcherdt, R. D., & Gibbs, J. F. (1976). Effects of local geological conditions in the San Francisco Bay region on ground motions and the intensities of the 1906 earthquake. *Bulletin of the Seismological Society of America*, 66(2), 467-500.

Bouchon, M. (1982). The complete synthesis of seismic crustal phases at regional distances. *Journal of Geophysical Research: Solid Earth*, 87(B3), 1735-1741.

Boyd, O. S., Jones, C. H., & Sheehan, A. F. (2004). Foundering lithosphere imaged beneath the southern Sierra Nevada, California, USA. *Science*, *305*(5684), 660-662.

Buehler, J. S., & Shearer, P. M. (2017). Uppermost mantle seismic velocity structure beneath USArray. *Journal of Geophysical Research: Solid Earth*, *122*(1), 436-448.

Chen, Y., & Xie, J. (2017). Resolution, uncertainty and data predictability of tomographic Lg attenuation models—Application to southeastern

China. *Geophysical Journal International*, *210*(1), 166-183.

Chun, K. Y., West, G. F., Kokoski, R. J., & Samson, C. (1987). A novel technique for measuring Lg attenuation—results from eastern Canada between 1 to 10 Hz. *Bulletin of the Seismological Society of America*, 77(2), 398-419.

Der, Z. A., Marshall, M. E., O'Donnell, A., & McElfresh, T. W. (1984). Spatial coherence structure and attenuation of the Lg phase, site effects, and the interpretation of the Lg coda. *Bulletin of the Seismological Society of America*, *74*(4), 1125-1147.

Eberhart-Phillips, D., & Michael, A. J. (1993). Three-dimensional velocity structure, seismicity, and fault structure in the Parkfield region, central California. *Journal of Geophysical Research: Solid Earth*, *98*(B9), 15737-15758.

Eberhart-Phillips, D., Thurber, C., & Fletcher, J. B. (2014). Imaging P and S attenuation in the Sacramento–San Joaquin delta region, northern California. *Bulletin of the Seismological Society of America*, 104(5), 2322-2336.

Eberhart-Phillips, D. (2016). Northern California Seismic Attenuation: 3D QP and QS Models. *Bulletin of the Seismological Society of America*, 106(6), 2558-2573.

Erickson, D., McNamara, D. E., & Benz, H. M. (2004). Frequency-dependent Lg Q within the continental United States. *Bulletin of the Seismological Society of America*, *94*(5), 1630-1643.

Farrar, C. D., & Bertoldi, G. L. (1988). Region 4, central valley and pacific coast ranges. Hydrogeology. *The Geological Society of North America, Boulder Colorado. 1988. p 59-67. 4 fig, 28 ref.*

Ford, S. R., Dreger, D. S., Mayeda, K., Walter, W. R., Malagnini, L., & Phillips, W. S. (2008). Regional attenuation in northern California: A comparison of five 1D Q methods. *Bulletin of the Seismological Society of America*, *98*(4), 2033-2046.

Gallegos, A., Ranasinghe, N., Ni, J., & Sandvol, E. (2017). Lg attenuation, frequency dependence and relative site response of the western United States as revealed by the EarthScope Transportable Array. *Geophysical Journal International*, 209(3), 1955-1971.

Gavin, P. (2019) The Levenberg-Marquardt algorithm for nonlinear least squares curve-fitting problems: Department of Civil and Environmental Engineering. *Duke University*, 10(1).

Godfrey, N. J., Beaudoin, B. C., & Klemperer, S. L. (1997). Ophiolitic basement to the Great Valley forearc basin, California, from seismic and gravity data: Implications for crustal growth at the North American continental margin. *Geological Society of America Bulletin*, 109(12), 1536-1562.

Godfrey, N. J., & Klemperer, S. L. (1998). Ophiolitic basement to a forearc basin and implications for continental growth: The Coast Range/Great Valley ophiolite, California. *Tectonics*, *17*(4), 558-570.

Hasegawa, H. S. (1985). Attenuation of Lg waves in the Canadian Shield. *Bulletin of the Seismological Society of America*, 75(6), 1569-1582.

He, J., Sandvol, E., Wu, Q., Gao, M., Gallegos, A., Ulziibat, M., & Demberel, S. (2017). Attenuation of regional seismic phases (Lg and Sn) in Eastern Mongolia. *Geophysical Journal International*, 211(2), 979-989.

Hong, T. K. (2010). Lg attenuation in a region with both continental and oceanic environments. *Bulletin of the Seismological Society of America*, *100*(2),

851-858.

Jennings, C.W., Strand, R.G., and Rogers, T.H., (1977), Geologic map of California: California Division of Mines and Geology, scale 1:750,000.

Jiang, C., Schmandt, B., Hansen, S. M., Dougherty, S. L., Clayton, R. W., Farrell, J., & Lin, F. C. (2018). Rayleigh and S wave tomography constraints on subduction termination and lithospheric foundering in central California. *Earth and Planetary Science Letters*, 488, 14-26.

Kennett, B.L.N. (1983) *Seismic Wave Propagation in Stratified Media*, Cambridge University Press, Cambridge, England.

Kennett, B. L. N. (1986). Lg waves and structural boundaries. *Bulletin of the Seismological Society of America*, *76*(4), 1133-1141.

Knopoff, L., Schwab, F., & Kauselt, E. (1973). Interpretation of Lg. *Geophysical Journal International*, *33*(4), 389-404.

Levenberg, K. (1944). A method for the solution of certain non-linear problems in least squares. *Quarterly of applied mathematics*, 2(2), 164-168.

Madsen K., Nielsen H.B., Tingleff O. (2004) *Methods for Non-Linear Least Squares Problems*, 2nd Ed., Informatics and Mathematical Modelling Technical University of Denmark.

Marquardt, D. W. (1963). An algorithm for least-squares estimation of nonlinear parameters. *Journal of the society for Industrial and Applied Mathematics*, 11(2), 431-441.

Mitchell, B. J., & Hwang, H. J. (1987). Effect of low Q sediments and crustal Q on *Lg* attenuation in the United States. *Bulletin of the Seismological Society of America*, *77*(4), 1197-1210.

Mitchell, B. J., Cong, L., & Jemberie, A. L. (2015). Continent-wide maps of Lg coda

Q for North America and their relationship to crustal structure and evolution. *Bulletin of the Seismological Society of America*, *105*(1), 409-419.

Mooney, W. D., & Kaban, M. K. (2010). The North American upper mantle: Density, composition, and evolution. *Journal of Geophysical Research: Solid Earth*, *115*(B12).

Noriega, R., Ugalde, A., Villaseñor, A., & Jurado, M. J. (2014). Spatial Variation of Lg-Wave Attenuation in the Iberian Peninsula. *Bulletin of the Seismological Society of America*, 105(1), 420-430.

Noriega, R., Ugalde, A., Villaseñor, A., & Jurado, M. J. (2015). Spatial variation of Lg-wave attenuation in the Iberian Peninsula. *Bulletin of the Seismological Society of America*, *105*(1), 420-430.

Nuttli, O. W. (1973). The Mississippi Valley earthquakes of 1811 and 1812: Intesities, ground motion and magnitudes. *Bulletin of the Seismological Society of America*, 63(1), 227-248.

Oliver, J., Press, F., & Ewing, M. (1954). Two-dimensional model seismology. *Geophysics*, 19(2), 202-219.

Page, B. M. (1981). The southern Coast Ranges, in *The Geotectonic Development of California* (Rubey Volume 1),W. G. Ernst (Editor), Prentice-Hall, Englewood Cliffs, New Jersey, 329–417.

Phillips, W. S., & Stead, R. J. (2008). Attenuation of Lg in the western US using the USArray. *Geophysical Research Letters*, *35*(7).

Pikser, J. E., Forsyth, D. W., & Hirth, G. (2012). Along-strike translation of a fossil slab. *Earth and Planetary Science Letters*, *331*, 315-321.

Poland, J. F., & Evenson, R. E. (1966). Hydrogeology and land subsidence, great

Central Valley, California. *Geology of northern California: California Division of Mines and Geology Bulletin, 190*, 239-247.

Ranasinghe, N. R., Gallegos, A., Hearn, T., Ni, J., & Sandvol, E. (2018). Frequency-dependent Lg attenuation in Northeast China and its implications. *Geophysical Journal International*, *212*(3), 2131-2142.

Rogers, A. M., J. C. Tinsley, W. W. Hays, and K. W. King (1979). Evaluation of the relation between near-surface geologic units and ground response in the vicinity of Long Beach, California, *Bull. Seism. Soc. Am*. 69, 1603-1622.

Ryan, W.B.F., S.M. Carbotte, J.O. Coplan, S. O'Hara, A. Melkonian, R. Arko, R.A. Weissel, V. Ferrini, A. Goodwillie, F. Nitsche, J. Bonczkowski, and R. Zemsky (2009), Global Multi-Resolution Topography synthesis, *Geochem. Geophys. Geosyst*., 10, Q03014.

Schutt, D. L., Lowry, A. R., & Buehler, J. S. (2018). Moho temperature and mobility of lower crust in the western United States. *Geology*, *46*(3), 219-222.

Shen, W., Ritzwoller, M. H., & Schulte-Pelkum, V. (2013). A 3-D model of the crust and uppermost mantle beneath the Central and Western US by joint inversion of receiver functions and surface wave dispersion. *Journal of Geophysical Research: Solid Earth*, *118*(1), 262-276.

Singh, S., & Herrmann, R. B. (1983). Regionalization of crustal coda Q in the continental United States. *Journal of Geophysical Research: Solid Earth*, *88*(B1), 527-538.

Su, F., Aki, K., Teng, T., Zeng, Y., Koyanagi, S., & Mayeda, K. (1992). The relation between site amplification factor and surficial geology in central California. *Bulletin of the Seismological Society of America*, 82(2), 580-602.

Tape, C., Plesch, A., Shaw, J. H., & Gilbert, H. (2012). Estimating a continuous Moho surface for the California unified velocity model. *Seismological Research Letters*, *83*(4), 728-735.

Tsai, Y. B., & Aki, K. (1969). Simultaneous determination of the seismic moment and attenuation of seismic surface waves. *Bulletin of the Seismological Society of America*, *59*(1), 275-287.

Unsworth, M.J. & Bedrosian, P., (2004) Electrical Resistivity structure at the SAFOD site from magnetotelluiric exploration, *Geophys. Res. Lett.*, 31, L12S05.

U.S. Geological Survey, California Geological Survey and Nevada Bureau of Mines and Geology, Quaternary fault and fold database for the United States, accessed October 12, 2019, at: https://www.usgs.gov/natural-hazards/earthquake-hazards/faults.

U.S. Geological Survey Volcano Hazards Program, U.S. Volcanoes and Current Activity Alerts, accessed January 2, 2020, at: https://volcanoes.usgs.gov/index.html.

Wang, Y., Forsyth, D. W., Rau, C. J., Carriero, N., Schmandt, B., Gaherty, J. B., & Savage, B. (2013). Fossil slabs attached to unsubducted fragments of the Farallon plate. *Proceedings of the National Academy of Sciences*, *110*(14), 5342-5346.

Wei, Z., Kennett, B. L., & Zhao, L. F. (2017). Lg-wave attenuation in the Australian crust. *Tectonophysics*, 717, 413-424.

Worden, C. B., D. J. Wald, J. Sanborn, and E. M. Thompson, 2015, Development of an open-source hybrid global Vs30 model, Seismological Society of America Annual Meeting, 21-23 April, Pasadena, California.

Xie, J., Gok, R., Ni, J., & Aoki, Y. (2004). Lateral variations of crustal seismic attenuation along the INDEPTH profiles in Tibet from Lg Q inversion. *Journal of Geophysical Research: Solid Earth*, *109*(B10).

Xie, J., & Mitchell, B. J. (1990a). A back-projection method for imaging large-scale lateral variations of Lg coda Q with application to continental Africa. *Geophysical Journal International*, *100*(2), 161-181.

Xie, J., & Mitchell, B. J. (1990b). Attenuation of multiphase surface waves in the Basin and Range province, part I: Lg and Lg coda. *Geophysical Journal International*, *102*(1), 121-137.

Yang, X. (2002). A numerical investigation of L g geometrical spreading. *Bulletin of the Seismological Society of America*, 92(8), 3067-3079.

Yassminh, R., Gallegos, A., Sandvol, E., & Ni, J. (2019). Investigation of the Regional Site Response in the Central and Eastern United StatesInvestigation of the Regional Site Response in the Central and Eastern United States. *Bulletin of the Seismological Society of America*, *109*(3), 1005-1024.

Zandt, G., Gilbert, H., Owens, T. J., Ducea, M., Saleeby, J., & Jones, C. H. (2004). Active foundering of a continental arc root beneath the southern Sierra Nevada in California. *Nature*, *431*(7004), 41-46.

Zhang, H., & Thurber, C. (2005). Adaptive mesh seismic tomography based on tetrahedral and Voronoi diagrams: application to Parkfield, California. *Journal of Geophysical Research: Solid Earth*, 110(B4).

Zhao, L. F., Xie, X. B., He, J. K., Tian, X., & Yao, Z. X. (2013a). Crustal flow pattern beneath the Tibetan Plateau constrained by regional Lg-wave Q tomography. *Earth and Planetary Science Letters*, *383*, 113-122.

Zhao, L. F., Xie, X. B., Wang, W. M., Zhang, J. H., & Yao, Z. X. (2013b). Crustal Lg
attenuation within the North China Craton and its surrounding regions.
Geophysical Journal International, 195(1), 513-531.

Zhao, L. F., Xie, X. B., Wang, W. M., & Yao, Z. X. (2008). Regional seismic
characteristics of the 9 October 2006 North Korean nuclear test. *Bulletin
of the Seismological Society of America*, *98*(6), 2571-2589.

Zhao, L. F., Xie, X. B., Wang, W. M., Zhang, J. H., & Yao, Z. X. (2010). Seismic Lg-
wave Q tomography in and around Northeast China. *Journal of
Geophysical Research: Solid Earth*, 115(B8).

Zhao, L. F., & Mousavi, S. M. (2018). Lateral variation of crustal Lg attenuation in
eastern North America. *Scientific reports*, *8*(1), 1-16.

Data acquisition from CCSE (2015): Central California Seismic Experiment, Caltech,
Dataset, doi:10.7909/C3B56GVW

초   록

본 연구에서는 TSM(Two-Station Method) 방법을 활용하여 CCSE(Central California Seismic Experiment)관측망을 통과하는 대원상의 단면(A-A')을 따라 Lg Q값이 공간적으로 변화하는 양상을 네 개의 중심 주파수 0.75 Hz, 1 Hz, 2 Hz, 그리고 2.75 Hz를 중심으로 추정하였다. 각 관측소에서의 상대적인 부지 응답 역시 RTSM(Reverse Two-Station Method) 방법을 활용하여 구하였다.

분석에 사용된 46개 관측소들 중 34개의 관측소로부터 양의 부지 응답 값이 얻어졌고, 이는 주로 퇴적암의 존재와 같은 이 지역의 지질학적 특성과 관련되어있다. 부지 응답 추정에 있어 퇴적물의 두께보다는 표층의 암상이 더 주요한 영향을 미치는 것으로 보인다. 또한 부지 응답 값은 V_{S30}값 분포와 강한 음의 상관관계를 나타냈다.

이렇게 측정된 부지 응답 값을 이용하여 Lg Q값 추정치를 보정했다. 보정 결과 피크 값이 나타나는 위치가 변화하였는데, 이는 보정 과정이 표층의 특성을 효과적으로 제거하기 때문으로 보인다. 피크 위치의 변동은 높은 주파수(2 Hz & 2.75 Hz)에서보다 낮은 주파수(0.75 Hz & 1 Hz)에서 더 두드러졌다. 부지 응답에 대해 보정된 Q값으로부터 $Q(f) = (81 \pm 8)f^{(0.62 \pm 0.11)}$ 이라는 주파수 의존성을 얻을 수 있었고, 이는 지구조적으로 활발한 지역적 특성과 유체의 존재성을 반영한다. 또한, 본 연구에서는 보정된 Lg Q값의 변화를 다양한 지질학적 특성들과 비교해보았다. 보정을 거치면 퇴적물의 영향은 줄어드는 모습을 보였고, 이는 특히 낮은 주파수에서 두드러지게 관찰되었다. S파 속도 및 모호면 온도 분포와의 비교를 통해 각각의 주파수들이 다양한 깊이 영역을 나타낼 수 있음을 확인하였다.

마지막으로, 이 지역에서의 결과를 사크라멘토 분지 지역에서의 결과와 비교했다. 퇴적 분지에서는 두 지역에서 유사한 거동이 관찰되었다. 그러나 시에라 네바다 산맥 인근에서는 두 지역에서 상반되는 결과를 보였기 때문에 추후에 더 촘촘한 관측망을 이용한 추가적인 연구가 이루어질 필요가 있다.